Palaeogeography, Palaeoclimatology, Palaeoecology 625 (2023) 111685

Contents lists available at ScienceDirect

Palaeogeography, Palaeoclimatology, Palaeoecology

journal homepage: www.elsevier.com/locate/palaeo

Pliocene volcanic terrain of the South Caucasus as a missing link in Eurasian palaeobiogeography: Dating and palaeoenvironments of vertebrate assemblages of the Jradzor locality, Armenia

Sergei Lazarev [a,b,c,*], Lutz Christian Maul [d], Klaudia Kuiper [e], Damien Becker [b,a], Maia Bukhsianidze [f], Hayk Hovakimyan [g], Lilit Sahakyan [g], Davit Vasilyan [b,a]

[a] Department of Geosciences, University of Fribourg, Chemin du Musée 6, 1700 Fribourg, Switzerland
[b] JURASSICA Museum, Route de Fontenais 21, 2900 Porrentruy, Switzerland
[c] Department of Earth Sciences, Utrecht University, Princetonlaan 8A, 3584 CB Utrecht, the Netherlands
[d] Research Station of Quaternary Palaeontology Weimar, Senckenberg Research Institute, Am Jakobskirchhof 4, 99423 Weimar, Germany
[e] Department of Earth Sciences, Faculty of Science, Vrije Universiteit Amsterdam, De Boelelaan 1085, 1081HV Amsterdam, the Netherlands
[f] Georgian National Museum, Purtseladze Street 3, 0105 Tbilisi, Georgia
[g] Institute of Geological Sciences, National Academy of Sciences of the Republic of Armenia, Marshal Baghramyan Avenue 24a, 0019 Yerevan, Armenia

ARTICLE INFO

Editor: H Falcon-Lang

Keywords:
South Caucasus
Pliocene
MN15
Vertebrate fauna
Pyroclastic density currents

ABSTRACT

Cenozoic faunal exchanges between Europe, Asia, Africa and America played a key role in shaping modern-day Eurasian ecosystems with dispersal pathways controlled by the dynamics of natural palaeogeographic barriers (e.g., deserts, isthmuses, large water bodies, etc.). The South Caucasus is a mountainous region between Asia and Europe, which served as an important dispersal route during the late Cenozoic for the intercontinental exchanges of diverse terrestrial vertebrates. The Pliocene geology of this region is dominated by volcanic and volcaniclastic deposits that are generally not favourable for fossil preservation. However, a few rich fossil vertebrate faunas do occur although they lack comprehensive palaeoenvironmental and age constraints. In this paper, we present an integrated study of the stratigraphy and palaeontology of the Jradzor section located in the Gegham volcanic province of Armenia, to improve knowledge of late Cenozoic dispersal pathways. The 57-m-thick succession comprises 19 fossiliferous horizons with at least 48 identified vertebrate taxa (excluding birds). The palaeoenvironmental reconstruction suggests that the succession was deposited within a short-lived dammed lake that was subject to pyroclastic density flows, and later evolved into soil catenas. Taphonomic observations indicate that pyroclastic flows caused a high mortality of small-size vertebrates in most fossiliferous horizons, while a catastrophic lahar buried the large vertebrate fauna. Multiproxy dating places the studied section between 4.3 and ~ 3.03 Ma and the mammalian fauna correlates to the MN15. Comparison with similar age localities from across the region shows that Jradzor comprises the most continuous Pliocene succession with the highest number of fossil taxa and fills the MN15 interregional gap. The rich fossil vertebrate faunas have Asian and primarily European affinities. Findings show that the South Caucasus was a significant dispersal route for terrestrial vertebrates between Europe, Asia and Africa, and is of crucial importance for understanding Eurasian palaeogeography.

1. Introduction

The faunal exchanges between Europe, Asia, Africa and America, known throughout the entire Cenozoic history, were controlled by the dynamics of intercontinental palaeogeographic and climatic barriers such as deserts, isthmuses, large water bodies, mountains, etc. (Demeter and Bae, 2020; Jiang et al., 2019; O'Dea et al., 2016). Among these, the late Cenozoic African-Eurasian fauna dispersal history is of the highest interest due to the involvement of Miocene apes and early humans (Bar-Yosef and Belfer-Cohen, 2001; Gabunia et al., 2010; O'Regan et al., 2011).

During the latest Miocene–early Late Pliocene (5.6–3.3 Ma), the

* Corresponding author at: Department of Geosciences, University of Fribourg, Chemin du Musée 6, 1700 Fribourg, Switzerland.
E-mail address: sergei.lazarev@unifr.ch (S. Lazarev).

https://doi.org/10.1016/j.palaeo.2023.111685
Received 4 January 2023; Received in revised form 9 June 2023; Accepted 11 June 2023
Available online 14 June 2023

Arabian desert underwent a phase of hyperaridification (the Neogene Arabian Desert Climax or NADX) that presumably terminated the Eurasian-African faunal exchange leading to the Pliocene endemism of the African ecosystems (Bibi, 2011; Böhme et al., 2021; Gibert et al., 2022). However, except for these geochemical and modelling studies, the evidence of such palaeogeographic disconnection in the fossil fauna record remains unclear, mainly due to the rarity of Pliocene rich and well-dated vertebrate localities in the regions neighbouring Arabia.

The South Caucasus (a geographic region roughly corresponding to territories of modern-day Armenia, Georgia, Azerbaijan and easternmost Turkey) is a mountainous region that, together with eastern Turkey on the west and Iran on the east, forms a biogeographic corridor between Asia, Europe and Africa (Fig. 1). Unique geographic location, variety of natural landscapes and mild climate made the South Caucasus a shelter for diverse ecosystems and endemic life forms (Nakhutsrishvili et al., 2015; Tarkhnishvili, 2014). The available studies also suggest that in the late Cenozoic, the region was an important tying point for the intercontinental dispersal of different vertebrate groups, including Miocene apes and early humans (Adler et al., 2014; Adler et al., 2008; Böhme et al., 2021; Derevianko et al., 2015; Gabunia et al., 2010; Gabunia et al., 2000; Kandel et al., 2017; Lordkipanidze et al., 2013). Nevertheless, while the Late Miocene and Quaternary geological and fossil records of the South Caucasus have been relatively well understood (Adamia et al., 2010; Antonosyan et al., 2019; Bukhsianidze and Koiava, 2018; Joannin et al., 2010), the Pliocene epoch in this respect is still unexplored and nearly unknown.

During the Pliocene, the South Caucasus, together with eastern Turkey and Iran, was a highly active volcanic region with a geological record consisting primarily of volcanic and volcaniclastic deposits (Fig. 1) (Adamia et al., 2010; Lechmann et al., 2018). Although volcaniclastic deposits (pyroclastic and other primarily fragmented volcanic rocks) are volumetrically the most abundant deposits of volcanic terrains, they have limited preservation potential for fossil vertebrates (Cas and Wright, 1987; Suthren, 1985). Being formed by rapid and

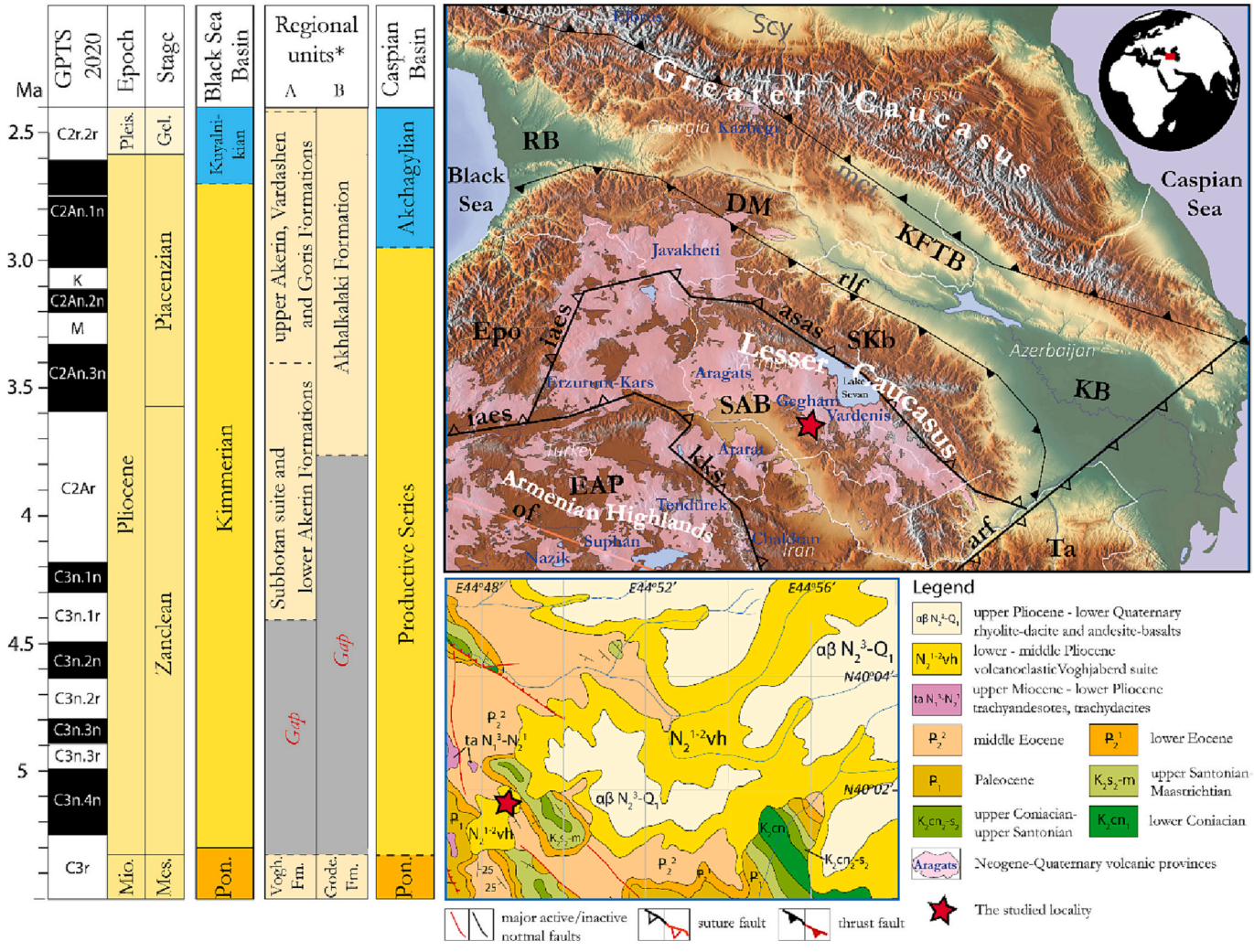

Fig. 1. Geological time scale and position of the Jradzor section in topographic map of the South Caucasus and geological map of the Lesser Caucasus. Columns from left to right: Global polarity time scale (GPTS) and time scale (GTS) (Raffi et al., 2020); Regional time scale for the Black Sea Basin (modified after Krijgsman et al., 2019); Regional stratigraphic units: A. of the Javakheti volcanic province in Georgia (modified after (Lebedev et al., 2008); B. of the Gegham volcanic province in the Lesser Caucasus; *Regional time scale for the Caspian Sea Basin (modified after Lazarev et al., 2021). Upper right corner – topographic map of the Caucasus (the map is taken from www.maps-for-free.com) with indicated regional tectonic-structural elements (modified after van Hinsbergen et al., 2020) and distribution of the late Cenozoic volcanic rocks (modified after Lechmann et al., 2018). Lower right corner – geological map of the studied area (Avanesyan, 2014). Abbreviations: Scy – Scythian Platform; RB -Rioni Basin, DM – Dzirulian Massif, KFTB – Kura Fold-Thrust Belt, KB – Kura Basin, mct – Main Caucasus Thrust, rlf – Racha-Lechkhumy Fault, SKb – Somkhet-Karabakh Island arc belt, Epo – Eastern Pontides, SAB – South Armenian Block, asas – Amasia-Sevan-Akera Suture, iaes – Izmir-Ankara-Erzinka suture, Ta – Talysz, arf – Araks Fault, kks - Kagızman-Khoy Suture (or Khoy obduction (Avagyan et al., 2017), EAP – East Anatolian Plateau, of – obduction front of the Arabian Plate (Nikogosian et al., 2023; Rolland et al., 2020; van Hinsbergen et al., 2020).

occasionally catastrophic events, the unconsolidated volcaniclastic deposits often become quickly eroded and thus, complete and continuous volcaniclastic deposits are rare. Because of that, the fossil record and the palaeoenvironments in and around active volcanic terrains are still one of the less studied. Therefore, any fossil findings in such regions are an exclusive exception and provide unique and rare insights into past ecosystems (Harrison, 2011; Iurino et al., 2014; Jiang et al., 2014; Pe-Piper et al., 2019).

The major Pliocene volcaniclastic formations in the South Caucasus are known as the Voghjaberd Formation in Armenia and the Goderdzi and Akhalkalaki formations in Georgia (Lebedev et al., 2008; Vereshchagin, 1982) (Fig. 1). Here, volcaniclastics occasionally alternate with sedimentary rocks that contain rich vertebrate assemblages, e.g., in the localities Nurnus in Armenia (Melik-Adamyan et al., 1988) and Kisatibi in Georgia (Gabelaya, 1970), both of which are known for >100 years. However, the lack of radio-isotope dating, absence of unambiguously sufficient biostratigraphic markers and unclear spatial and temporal constraints of volcaniclastic formations largely leave the question on the age of these localities open.

The insufficient knowledge of the ages of the geological formations, the faunistic assemblages, and the depositional systems in the South Caucasus during the Pliocene hinders a comprehensive understanding and reconstruction of the geological past of the region, including the evolutionary history of the palaeoenvironment and biodiversity. Continuous explorations in Neogene continental deposits in Armenia now yielded a unique Pliocene continental record.

This paper presents our results on integrated stratigraphy (magnetostratigraphy, $^{40}Ar/^{39}Ar$ dating and sedimentology) and palaeontology of the 57-m long Jradzor section located in the foothill of the Gegham volcanic province, Armenia. The section, located in an actively explored diatomite-mine, consists of predominantly volcaniclastic rocks and has at least 19 fossiliferous horizons with at least 48 identified vertebrate taxa (excluding birds). In the Jradzor locality, fossil assemblages of fish, reptiles and large mammals have been reported before (Vasilyan, 2008a, 2008b). However, the age interpretations based on mammalian biochronology remained largely inaccurate, ranging from the late Miocene to Pliocene (Avakyan, 1963; Vasilyan and Bukhsianidze, 2020; Vasilyan and Carnevale, 2013).

The paper aims to reconstruct the palaeoenvironmental evolution and biotic record of the Jradzor section that represents the Pliocene volcanic terrain of the South Caucasus. At a smaller scale, this study will help to better understand the taphonomy and preservation potential of vertebrate remains in volcanic regions. In a larger context, our paper will shed light on the palaeobiogeographic role of the South Caucasus in the ecosystem interaction between Asia, Europe and Africa during the Pliocene. Improved solid age constraints for the fossil findings will allow further palaeontological, palaeobiogeographic and palaeoclimatic studies in this region.

2. Geological background

2.1. Jradzor section

The Jradzor section is located in the SW part of the Gegham volcanic province of the Lesser Caucasus. It is situated in an active diatomite mine, 13 km to *E*-NE from the Narek village, Central Armenia at an altitude of 1930 m a.s.l. (40°1′42.53"N 44°48′53.92″E) (Fig. 1). The diatomite reserves were discovered in the 1960s (Avakyan, 1963), while the active exploration began in the 2000s. Although the Jradzor section has been previously reported as a palaeontological locality by findings of fish, reptiles and mammals, accurate dating and reconstruction of the depositional environments of the locality have not yet been performed (Vasilyan, 2008a, 2008b; Vasilyan and Bukhsianidze, 2020; Vasilyan and Carnevale, 2013).

2.2. The Lesser Caucasus and Gegham volcanic province

The Lesser Caucasus (in its geological meaning), being the easternmost part of the Armenian Highland, is located south of the Greater Caucasus mountains and separated from it by the Variscian metamorphic Dzirulian Massif and two foreland basins – the Kura Basin in the east and the Rioni Basin in the west (Fig. 1). The NW-SE-trending orogenic belt of the Lesser Caucasus, from the NE to SW comprises three major lithostructural domains: 1. The Eurasian margin represented by the Somkhet-Karabakh island arc belt; 2. The Jurassic ophiolitic Sevan-Akera-Amasia suture zone; 3. The Gondwana-derived microcontinent known as the South Armenian Block (SAB) (Nikogosian et al., 2023; Sahakyan et al., 2017; Sosson et al., 2010).

The Lesser Caucasus evolved as a product of continuous closure of the northern Neotethys Ocean (during Middle Jurassic–Cretaceous), followed by collision of the SAB with the Eurasian margin (during Late Cretaceous–Palaeocene) and eventually by the amplified Arabian-SAB-Eurasian collision (during Late Eocene–present) (Rolland, 2017; Sahakyan et al., 2017; Sosson et al., 2010; van Hinsbergen et al., 2020). Subduction and collision resulted in active volcanism by which vast territories of Turkey, NW Iran and Lesser Caucasus were covered with volcanic and volcaniclastic rocks making this area one of the most active Cenozoic volcanic areas on land (Fig. 1) (Lechmann et al., 2018; Navasardyan, 2006; Neill et al., 2015; Rolland, 2017; Sosson et al., 2010).

The Gegham volcanic province is a Late Miocene–Quaternary volcanic plateau in Central Armenia, located to the west of Lake Sevan (Fig. 1). The geochemical and geochronological study of volcanic rocks in Gegham revealed three intervals with distinct volcanic activities: 1. Late Miocene–Early Pliocene (5.56–4.7 Ma); 2. Late Pliocene-Early Pleistocene (3.5–1.9 Ma); 3. Middle–Late Pleistocene (0.9–0.01 Ma) (Lebedev et al., 2021). The majority of lavas in all intervals is represented by mildly alkaline rocks with compositions varying from trachybasalts to trachydacite, and locally to rhyolites (Arutyunyan et al., 2007; Karapetyan and Adamyan, 1973; Lebedev et al., 2021; Lebedev et al., 2018; Meliksetian, 2018; Sugden et al., 2021). The Pliocene volcanism, accompanied by the overall uplift of the region, has been attributed to the delamination of the SAB lithospheric mantle weakened by asthenospheric upwelling (Lebedev et al., 2021; Lechmann et al., 2018; Rolland, 2017; Sosson et al., 2010), to amphibole dehydration melting (Allen et al., 2013), or various combinations of these factors (Neill et al., 2015; Sugden et al., 2019).

2.3. Palaeoclimatic and -geographic context of the South Caucasus

During the Pliocene, the global climate transformed from relatively warm and stable to more extreme and colder in the Pleistocene (de Schepper et al., 2014). Among the most remarkable Pliocene climatic events are the onset of the Northern Hemisphere glaciation at 3.6 Ma, characterised by an expansion of glaciers in the Barents Sea, Alaska, North America and Iceland, and the mid-Piacenzian climatic optimum (3.26–3.02 Ma) when the rise of annual temperatures, and contraction of deserts and expansion of forests were detected globally (Haywood et al., 2016; de Schepper et al., 2014).

The intensity of the Pliocene palaeoclimatic events in the South Caucasus remains unknown. Geochemical data from the neighbouring region of Zagros Mountains (Western Iran) suggest a development of hyperarid environments on the Arabian Peninsula between 5.6 and 3.3 Ma that has been interpreted to be responsible for the termination of faunal exchanges between Africa and Eurasia (Böhme et al., 2021). The organic geochemistry data from the neighbouring region of the Caucasian foreland Kura Basin (Lokbatan section, Caspian Sea) suggest rather dry climatic settings and a gradual temperature decline between 3.6 and 3.2 Ma (Vasiliev et al., 2022).

3. Methodology

3.1. Logging and facies analysis

The Jradzor section has been measured using a geological compass and a portable Jacob's staff. The facies analysis is based on field observations on lithofacies, including a description focusing on colour, grain size, lithology and sedimentary structures, as well as the shape of beds, their distribution and relations between them. The descriptive terminology followed the field guide of Tucker (2012). The classification of lithological facies and facies associations used in our study follows the concept of Miall (1996) and Posamentier and Walker (2006).

For a better understanding of the facies distribution and tracing the relations between laterally variable beds, the quarry has been photographed with a portable drone DJI Mavic Air 2, and subsequently, a 3D model was generated with Agisoft software at the JURASSICA Museum (Porrentruy, Switzerland) (Fig. 2).

3.2. Magnetostratigraphy

For magnetostratigraphic dating, 73 standard cylindrical palaeomagnetic doublet-samples were taken across the entire section using a portable battery drill machine, diamond crones (Ø 25 mm) and a water tank with a pump. Each sample was oriented with a measuring table and compass. Additionally, a local declination of 6° (August 2018, https://www.ngdc.noaa.gov/geomag/calculators) has been added to the orientation measurements to compensate for secular variation. Palaeomagnetic measurements including thermal demagnetisation, demagnetisation in alternating field and thermomagnetic runs (Curie balance), were performed at the Paleomagnetic laboratory "Fort Hoofddijk", Utrecht University, the Netherlands. The methodology of measurements follows Lazarev et al. (2020).

The supplementary data associated with this paper contain a catalogue with information about all taken and analysed samples as well as an interpretation of palaeomagnetic data (directions and statistics) that can be uploaded on Paleomagnetism.org (Supplementary 1,2).

3.3. $^{40}Ar/^{39}Ar$ chronology

Five volcanic tephra samples (JZ-V1, JZ-V2, JZ-V3, JZ-V4, JZ-V5, Fig. 2) have been dated using $^{40}Ar/^{39}Ar$ geochronology. Samples are measured at the Vrije Universiteit Amsterdam on an Argus VI^{+} noble gas mass spectrometer. Analytical procedures are reported in the supplementary information. Ages are calculated with (Min et al., 2000) decay constants and 28.201 Ma for FCs (Kuiper et al., 2008). The atmospheric $^{40}Ar/^{36}Ar$ air value of 298.56 is used (Lee et al., 2006). All errors are quoted at the 2σ level. Note that we analysed ~10 grains per fusion, since single-grain measurements do not yield sufficient argon gas. This implies that data should be interpreted as a maximum age (i.e. depositional age is similar or younger) since samples can suffer from (xenocyrstic) contamination of older grains that might go unnoticed in multiple grain samples. We report two ages based on: Approach 1 – the youngest age population where MSWD < *t*-test at 95% confidence; Approach 2 – the age population including most analyses with MSWD <

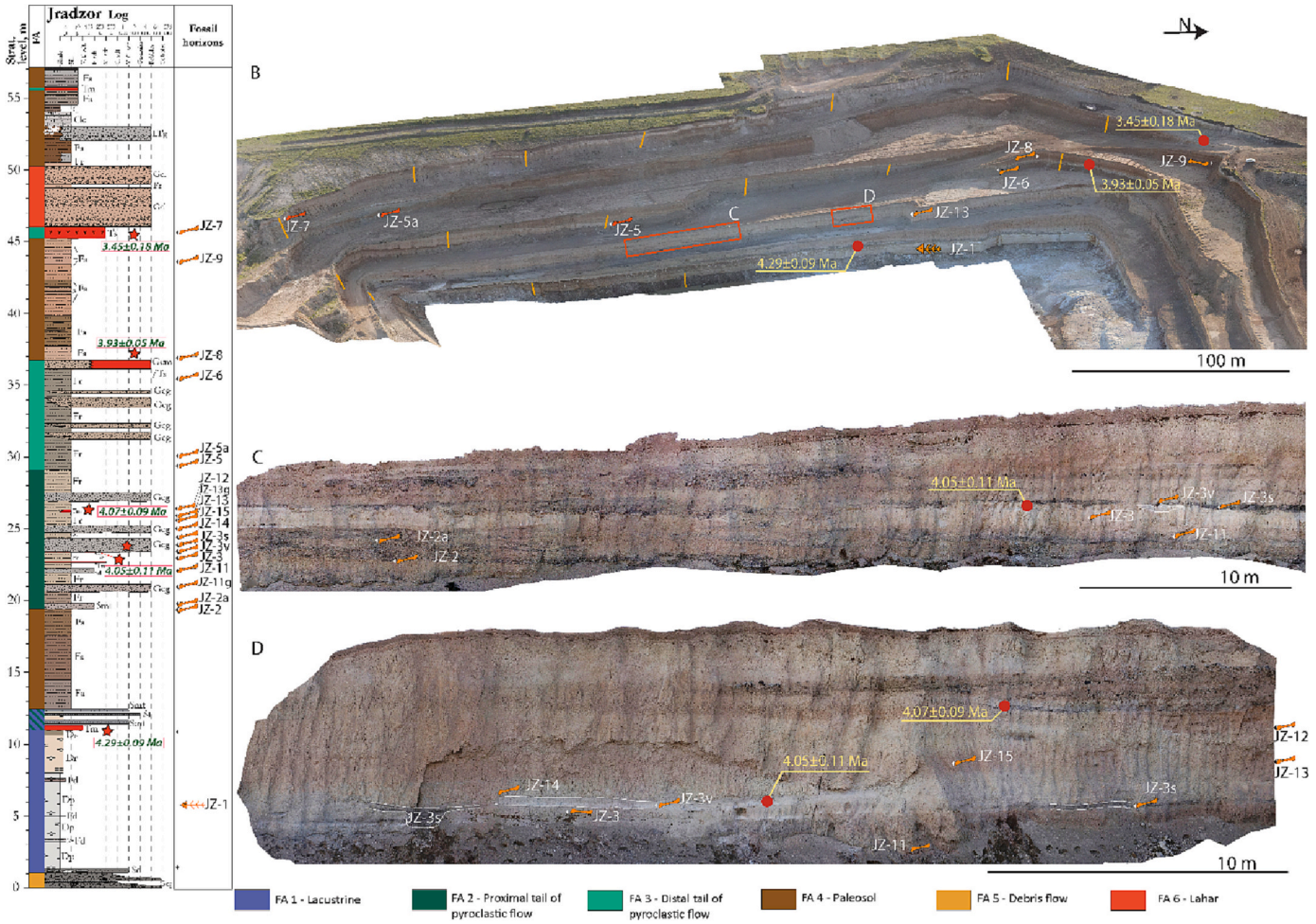

Fig. 2. Composite log of the Jradzor section (A) and 3D models of the quarry (B) and some parts of the quarry walls (C, D) with indication of fossil horizons, $^{40}Ar/^{39}Ar$ dates and logging paths (orange lines on model B).

t-test at 95% confidence (see 4.3). All relevant analytical data for age calculations can be found in the supplementary data (Supplementary 3, 4).

3.4. Palaeontology

The fossil vertebrate remains were collected directly from the layers, and information about preliminary identification, stratigraphic level and taphonomic situation was documented. A small amount of fossil material originates from a screen-wash prospection to estimate the potential of sediments for vertebrate remains. Screen-washing of nearly all fossiliferous horizons was not productive, as the strongly lithified and welded fossil-bearing volcaniclastic rocks appeared to be very resistant to chemical treatment with hydrogen peroxide and/or acetic (or any) acid. The only exception is the pedogenically-modified sediments from the fossil horizon JZ-6 (35.5–36.2 m) that disintegrated with hydrogen peroxide.

The identification of the vertebrate fossil specimens was based on comparative anatomy through the observation, measurement and comparison of anatomical characters. For that, the collection of fossil and recent fauna material stored at the Jurassica Museum (Porrentruy, Switzerland) and the Research Station of Quaternary Palaeontology (Weimar, Germany) and literature sources were used. The resulting taxonomic framework is a list of all currently identified fossil fauna (Supplementary 5).

The correlation of the mammalian faunas to the MN units follows the approach described by Raffi et al. (2020). The ages of fossil horizons were also calculated using the $^{40}Ar/^{39}Ar$ ages of located in between volcanic tephra and further, narrowed down using the position of fossil horizons in certain magnetic polarity chrons.

The fossil material described in this paper belongs to the palaeontological collections of the Institute of Geological Sciences (IGS) and Institute of Botany (IB), both belong to the National Academy of Sciences of the Republic of Armenia, Yerevan, Armenia.

4. Results

4.1. Sedimentary facies, facies associations and associated fossils

In the 57 m thick succession, we distinguished 17 lithological facies formed by various depositional processes (Table 1). Lithofacies were grouped into six facies associations that represent distinct depositional environments.

4.1.1. Facies association 1 (FA1) – lacustrine

4.1.1.1. Description. The FA1 occupies the lower part of the section (1.3–11 m) and represents various facies of diatomite with rare thin beds of sandstones and mudstones (Fig. 3A). Thinly parallel-laminated diatomite (Dh) with white laminae of 1–7 mm-thick prevails in the lowermost part of the FA1 (1.3–8 m, Fig. 3B). On average, there are 300–320 laminae per meter of the Dh facies. The Dh contains partial and complete small- to large-sized fish and amphibian skeletons and rare finds of isolated skeletal elements of tortoise and small mammals (Fossil horizon JZ-1, Fig. 3C). Inside the Dh, infrequent sharp-based 3–10 cm-thick beds of brown mudstone (Fd) and sandstone (Sd) occur, both with white rounded diatomite intraclasts (Fig. 3D).

Towards the top (8–11 m), the Dh gradually transforms into a brown stratified diatomite with occasional lenticular bedding (Dr) (Fig. 3E). Towards the south (left part of the western (main) wall), the Dr. laterally converts into a dark grey parallel-stratified speckled diatomite (Ds) with disarticulated amphibian and small-sized fish fossils as well as occasion sedge-like plant imprints between 10.65 m and 11 m. The speckles represent white rounded diatomite intraclasts of up to 1 cm big (Fig.3F).

In the southern part of the quarry, between 11.5 m and 12.5 m, thin beds of grey diatomite alternate with thin beds of volcaniclastic sandstones and tephra belonging to FA2. This alternation, however, is not present in the central part of the quarry, where the Dr. is followed by breccia of FA2 with a sharp and irregular contact.

4.1.1.2. Interpretation. The FA1 is interpreted as representing a shallowing-upwards lacustrine environment occasionally affected by exceptional inflow (flood) events. The thinly-laminated diatomite (Dp) was deposited by a seasonally-mediated accumulation of diatoms (white lamina) progressively followed by a minor clastic input from suspension fallout (light brown tops of laminae) in a stable water column (Dean and Fouch, 1983; Lindqvist and Lee, 2009; Sáez et al., 2007). The rare beds of mudstone and sandstone (Fd, Sd) with diatomite intraformational clasts represent relatively dense sediment-laden gravity flows, which eroded the basin bottom, incorporating the diatomite clasts into the current (Lindqvist and Lee, 2009; Sasaki et al., 2016). General pyritization of the fish remains and accumulation in a stable water column suggest poorly-oxygenated environments.

The lenticular bedding with occasional symmetrical (wave) ripples in the upper diatomite (Dr) points at increased depositional energy triggered by wave activity and/or winnowing (Raaf et al., 1977). The grey diatomite with intraclasts and plant imprints is indicative of the nearshore zone with even stronger wave activity and the presence of aquatic vegetation.

The overall sedimentological profile in the FA1 has a shallowing trend from a stable, relatively deep-water setting to a nearshore wave-prone environment. Assuming that the diatomite laminae represent annual layers, the lacustrine phase of the section lasted for about 2000–3000 years.

Similar lithofacies and facies association were reported as lacustrine offshore in the Holocene-Pleistocene record of the Lake Chungará in Chile (Sáez et al., 2007), as lacustrine in the Pleistocene Guayllabamba Basin in the Ecuadorian Andes (Martin-Merino et al., 2021) and as lacustrine facies in the Early Miocene Foulden Maar in New Zealand (Lindqvist and Lee, 2009).

4.1.2. Facies association 2 (FA2) – medium tail of pyroclastic flow (pyroclastic flows, ground-surges and ash-cloud surges)

4.1.2.1. Description. The FA2 is formed by sharp-based winged incisions of up to 35 m wide and 1 m thick that laterally demonstrate strong facies variation (Fig. 3G). The central parts of the incision forms U-shaped gullies that consist of welded, poorly-sorted, but generally normally-graded massive to trough cross-laminated cobble tuff breccia (Gcg) gradually passing upwards into massive to scarcely-laminated poorly-sorted tuffaceous sandstones (Smt) (Fig. 3H, I). The wings of incisions are composed of either Smt or locally (11.5–12.5 m) of trough-cross-laminated poorly-sorted coarse-grained tuffaceous sandstones (St) and both frequently change laterally into a white massive volcanic tuff (Tm) (Fig. 3J).

The incisions are mantled by up to 0.7 m-thick beds of tuffaceous rootled mudstones (Fr) with gradual contact. Stratigraphically higher incisions usually reside into the Fr-facies from previous incisions and the facies order Gcg > Smt > Fr repeats. However, locally incisions may cut through sharp-based parallel-laminated volcanic ash (Ts, up to 0.3 m thick) or through white reversely-graded lapilli tuff (LTg) up to nearly complete erosion of the underlying layer, with only separated lenses present in the section (Fig. 3K). In two incisions across the section, the Fr mudstones are covered by white poorly-sorted normally-graded lapilli tuff (LTg), gradually fining upwards into a massive, very fine-grained tuff (Tm).

The Fr-facies that mantles the incisions towards the margins of the depression becomes more pedogenically-modified and rootled and form a conformable sequence of Fr-facies lying on top of each other with straight or irregular contacts.

Table 1
Description of lithological facies recognised in the Jradzor section and interpretation of depositional processes associated with them. The facies codes were modified after Miall (1996) and Chough (2013).

Code	Grain size	Sedimentary structures	Occurrence	Depositional process	Figure
Gcg	Clast-supported cobble tuff breccia	Normally-graded poorly-sorted, locally through cross-bedded and welded tuff breccia with irregular base. Very angular (Category 0 by Tucker, 2012) clasts of andesites/dacites with sizes from 0.04 to 0.25 m, locally with boulders up to 0.5 m.	When not welded: 1. Gcg-facies with blocks up to 1 m constitutes hummocky-shaped hill of up to 35 m thick and > 120 m wide that rests at the base of the section; 2. Up to 0.8-m-thick sheet beds alternating with Gct; When welded: 3. Central parts (U-shape gullies) of 0.3–1 m thick and up to 35 m wide winged incisions where it is associated with Smt, St and Fr; 4. Incisions of up to 10 m wide and 0.7 m thick where Gcg is associated with Smt and Tm; 5. Sheet beds of up to 8 m wide and 0.4 m thick occur among Fr-facies.	1 and 2. Deposition *en masse* from fluid-saturated cohesive flow induced by collapse of volcanic edifice (Siebert, 1984). 3–5. Gravitational segregation of high-density lithics in axial part of hot highly-concentrated gas/particle gravity-controlled flow induced by volcanic activity (pyroclastic flow) (Cas and Wright, 1987; Tate and Wilson, 1988).	Fig. 3I, X
Gcm	Clast-supported pebble/cobble breccia	Massive, poorly-sorted breccia with straight or irregular base. Clast size varies between first mm to 20 cm. Roundness from very subangular (0) to rounded (4) (Tucker, 2012).	Locally, Gcm fills incisions of up to 3 m thick and 25 m wide; 2. Lenses of up to 5 m wide and 0.4 m thick among Fa; 3. Lenses of 0.3 m wide and 0.1 m thick among Fa.	Pseudoplastic debris flows (inertial bedload) (Miall, 1996).	Fig. 3Z
Gct	Clast-supported granule gravel	Moderately sorted, trough cross-stratified granule gravel with cross-set thickness of 0.1–0.3 m and up to 2 m wide. The base is irregular, locally straight.	Forms laterally-delimited layers in a 5-m-thick package in northern (secondary) wall, where it alternates with Gcg.	Reworking of mass flow deposits by minor channels/rills (Chough, 2013; Miall, 1996).	Fig. 3Y
Gcl	Clast-supported lapilli breccia	Massive, poorly-sorted breccia built of 60–95% of white 2–10 mm pumice lapilli in a brown highly porous muddy matrix, erosive base.	Massive bed from 3 m thick in the basin centre to 1 m on the margins Associated with Fr.	Distal residue of cohesive debris flow of pyroclastic material (lahar) (Cas and Wright, 1987; Chough, 2013).	Fig. 3A2
Smt	Medium- grained sandstone to granulite	Massive to scarcely laminated, medium to very coarse-grained tuffaceous sandstone with irregular base.	Forms small incisions up to 0.3 m thick and 3 m wide or constitutes wings of large, up to 35 m wideand 1 m thick incisions, where it has thickness up to 0.5 m. Associated with Gcg ang Fr; Locally eroded by St.	Gravitational segregation of lower density matrix in axial and peripheral parts of pyroclastic flows (Cas and Wright, 1987).	Fig. 3H, J, K, L
St	Coarse-grained sandstone, granulite	Poorly-sorted sandstone to granulite with trough cross-lamination in cross-sets of 1–5 cm-thick; Erosive base, unidirectional; Linear beds up to 0.2 m thick.	Locally (11.5–12.5 m) forms Associated with Fr. Laterally passes	Migration of sinuous-crested ripples, lower flow regime (Miall, 1996).	Sup. 6, Fig. 1.1
Sd	Coarse-grained to very coarse-grained sandstone	Poorly-sorted sandstone with angular irregularly-distributed pieces and blocks (up to 20 cm) of white diatomite, irregular base.	Linear beds with thickness of 0.3 m. Associated with Dh.	Erosion and downslope transportation of the basin margin/bottom by high-density gravity flow during exceptional inflow (flood) events (Lindqvist and Lee, 2009; Sáez et al., 2007).	Sup.6, Fig. 1.2
Dh	Diatomite	Horizontal lamination with thin (2–5 mm) laminae. Each lamina is sharp-based and gradually changes its colour upwards from white to light brown.	Continuous packages up to 4.5 m thick. Associated with Fd, Sd. Passes upwards into Ds, Dr.	Seasonal deposition of the diatom algae from suspension in stable water column (Lindqvist and Lee, 2009).	Fig. 3B
Ds	Diatomite	Dark grey diatomite with rounded intraformational clasts of white diatomite and gradational base.	Continuous package up to 3 m thick. Laterally transforms into Dr.	Erosion and downslope transportation of the basin margin/bottom by high-density gravity flow during exceptional inflow (flood) events. (Lindqvist and Lee, 2009; Sáez et al., 2007).	Fig. 3F
Dr	Diatomite	Brown diatomite, generally stratified but internally massive with implicit lenticular bedding represented by sandy symmetric ripples of up to 2 cm wide and 1 cm high. Gradational base.	Continuous package up to 3 m thick. Laterally transforms into Ds.	Deposition of the diatom algae in a nearshore zone affected by wave activity and/or winnowing (Raaf et al., 1977).	Fig. 3E
Ts	Very fine- to medium-grained volcanic ash	White, grey horizontally-laminated tuff composed of alternating finer and coarser layers. The basal surface is irregular while the intrabed surfaces are straight.	Linear but laterally disappearing beds of 0.3–0.6 m thick. Preceding or laterally passing into Gcg.	Transition from turbulent to traction type transport in low-concentration gas-solid dispersion (ground surge) (Fisher and Smith, 1991).	Fig. 3K
Tm	Fine- to medium-grained tuff	Grey, white, massive tuffs with irregular base.	Linear beds of 0.05 to 0.3 m thick. Laterally passes into Gcg or Fr.	Lateral extension of the Tm-facies from Gcg suggests accumulation in peripheral lower density parts of the pyroclastic flows.	Fig. 3J
LTg	Lapilli tuff	White normally-graded and reversely-graded lapilli tuff with pumice fragments from 1 mm to 1 cm and straight base and gradual bases.	Reversely-graded LTg forms rare beds up to 0.5 m-thick preceding the Gcg-breccia. Normally-graded LTg fills one incision of 10 m wide and up to 1 m thick.	Reversely-graded LTg: Buoyancy grading resulted from density contrast in confined pyroclastic flow with lower density vesiculated pumice floating in higher density matrix. Normally-graded LTg: Less-confined (more expanded) pyroclastic flows with matrix density lower than the pumice (Cas and Wright, 1987).	Fig. 3O

(*continued on next page*)

Table 1 (*continued*)

Code	Grain size	Sedimentary structures	Occurrence	Depositional process	Figure
Fr	Tuffaceous mudstone to tuff	A. Greenish-grey to white rootled tuffaceous mudstone with abundant mm- to cm-scale rootlets and carbonate nodules and concretions of 5–10 cm in size. B. Pale yellowish brown massive and porous tuffaceous mudstone to dense tuff, with dispersed angular fragment of volcanic lithics from 1 mm to 10 cm and scarce cm-scale rootlets.	A. Linear beds of 0.05–0.3 m thickness with gradational base; B. Linear beds of 0.1–0.8 m thickness with irregular base. Fr-facies mantles Gcg, Smt, St; Laterally may transform into Tm.	Accumulation *en masse* from the ash-cloud surge that accompanies the pyroclastic flow (Fisher, 1979) followed by paedogenic and aerial downslope washover modification.	Fig. 3P
Fa	Mudstone	Brown aggregate mudstone with mm-scale rootlets and dispersed mm-scale angular fragments of volcanic lithics. Locally, the mudstone is penetrated by cm-scale carbonate-infilled rootlets. The base surface is highly irregular, with frequent rounded cm-scale krotovinas.	Linear beds of 0.4–3 m thickness. Associated with Clc and C.	Pedogenesis with local small-scale reworking by rills (Sulpizio et al., 2006; Tabor et al., 2017).	Fig. 3T, U
Fd	Mudstone	Brown mudstone with small white diatomite intraclasts (up to 3 cm) and irregular base.	Linear beds of 3–10 cm thick, with sharp straight basal surface. Associated with Dh.	Generation of low-density slurry flows (Lindqvist and Lee, 2009).	Fig. 3D
C	Claystone	Brown sandy claystone with blocky to columnar structure, irregular base. Linear bed up to 0.5 m thick.	Underlain by Clc, succeeded by Fa.	Clay Illuvial horizon depleted in paedogenic carbonates (Tabor et al., 2017; Zamanian et al., 2016).	Fig. 3V
Clc	Calcrete	White massive to crudely laminated limestone depleted in clastic material; Gradual base with abundant cm-scale rootlets.	Forms 1-m-thick massive layer in the quarry centre that is thinning towards the quarry margins. Associated with Fa and C.	Impregnation and cementation of soil horizon with paedogenic carbonates from shallow groundwater table (Zamanian et al., 2016).	Sup.6. Fig. 1.3

The FA2 is extremely rich in fossil bones of small-sized vertebrates represented by irregularly-distributed remains of amphibians, reptiles, birds and mammals. The fossils mainly occur in the Gcg- and Fr-facies, where they are mostly disintegrated and welded with fragments of pumice. However, within the Fr-facies, remains with partial anatomical connections have been found (Fig. 3L).

4.1.2.2. Interpretation. The winged incision of the FA2 with tuff breccia (Gcg) > tuffaceous sandstone (Smt) in gullies and tuffaceous sandstones (Smt, St) > tuff/mudstone (Tm/Fr) on the wings are products of **pyroclastic flows –** hot, highly-concentrated gas-rich sediment gravity flows induced by explosive volcanic activity (Suthren, 1985). The pyroclastic flows generally bear such features as poor sorting, welding, high erosional capacity and strong topographic control, infilling valleys and depressions (Cas and Wright, 1987; Tate and Wilson, 1988).

The poorly-sorted gully-forming tuffaceous breccia (Gcg) represents the most destructive middle part of the flow, characterised by the maximum velocity and concentration of the biggest clasts (Tate and Wilson, 1988). The poor sorting is attributed to high particle concertation rather than to turbulency with the general flow mechanism being laminar or plug-like (Cas and Wright, 1987; Suthren, 1985). At the same time, the overall normal grading and transition from Gcg-breccia to Smt-sandstone stand for a gravitational control of the flow. The high content of volcanic tuff in Gcg-breccia and a generally welded character of the deposits indicate a high temperature of the flow. This is in agreement with the observed welding of numerous bone fragments with lapilli.

The lateral fining of the incisions correlates with a decrease of the gas/particle concentration towards the margins of the wedge-shape pyroclastic flows (Tate and Wilson, 1988). The occurrence of traction structures, such as occasional trough cross-lamination on the wings of incision, is linked to the migration of the sinuous-crested dunes that accumulated from small suspension clouds (Miall, 1996; Reading, 1996).

The tuffaceous rootled mudstone/tuff (Fr) that succeeds every pyroclastic flow and mantles topography much further away from the pyroclastic flows is interpreted as an **ash-cloud surge** – a cloud of expanded turbulent low-concentrated volcanic ash that accompanies pyroclastic flows and accumulates on top of them as the lightest fraction (Cas and Wright, 1987; Fisher and Smith, 1991). Development of vegetation in these mudstones expressed as mm-scale rootlets characterise periods of intervening repose between pyroclastic flows.

The lenses of parallel-laminated sharp-based volcanic ash, locally preceding the pyroclastic flows (Ts) are interpreted as the **ground-surge** deposits – those accumulated from a low-concentration lighter mixture of volcanic ash and gas that outpaces the pyroclastic flows and becomes covered/eroded by them (Tate and Wilson, 1988; Wohletz and Sheridan, 1979). This makes the ground-surge deposits of extremely low preservation potential (Suthren, 1985).

Similar pyroclastic deposits were reported from the Pleistocene deposits of the Lesser Antilles (Tate and Wilson, 1988) and the Holocene volcaniclastic succession of the São Roque volcano, Azore Islands (Zanon et al., 2009).

4.1.3. Facies association 3 (FA3) – distal tail of pyroclastic flow (pyroclastic flows and ash-cloud surges)

4.1.3.1. Description. The FA3 generally resembles the FA2, but the sharp-based breccia-built incisions are smaller and rare, and the mudstones covering them become greenish-grey and more rootled. The Gcg-breccia in such incisions becomes more sandier, and the cobble concertation is lower than in the Gcg-facies of the FA2. There are three types of incisions: 1. Incisions up to 10 m wide and 0.7 m thick built of poorly-sorted but generally normally-graded tuff breccia (Gcg). Laterally, towards the wings, breccia transforms into a poorly-sorted massive granulite (Smt) with frequent chaotically-distributed pebbles and cobbles or locally, into white massive (Tm) or parallel-laminated (Ts) sharp-based volcanic ash/tuff (Fig. 3M); 2. Incisions of up to 3 m wide and 0.3 m thick are constituted by poorly-sorted massive granulite (Smt). 3. At 52 m, one incision of up to 1 m thick and 10 m wide is filled with white normally-grading pumice lapilli (LTg, Fig. 3N, O).

Similar to FA2, incisions from the FA3 occupy the central part of the western (main) wall and trend in the NW-direction. Each incision is mantled by greenish-grey tuffaceous mudstone (Fr) with gradational contact. Mudstones comprise abundant cm-scale rootlets (Fig. 3P) with locally developed horizons of rounded carbonate nodules of up to 7 cm in size and carbonate concretions up to 20 cm in size (Fig. 3Q). The mudstones change their thickness from 0.2 cm in between the incisions

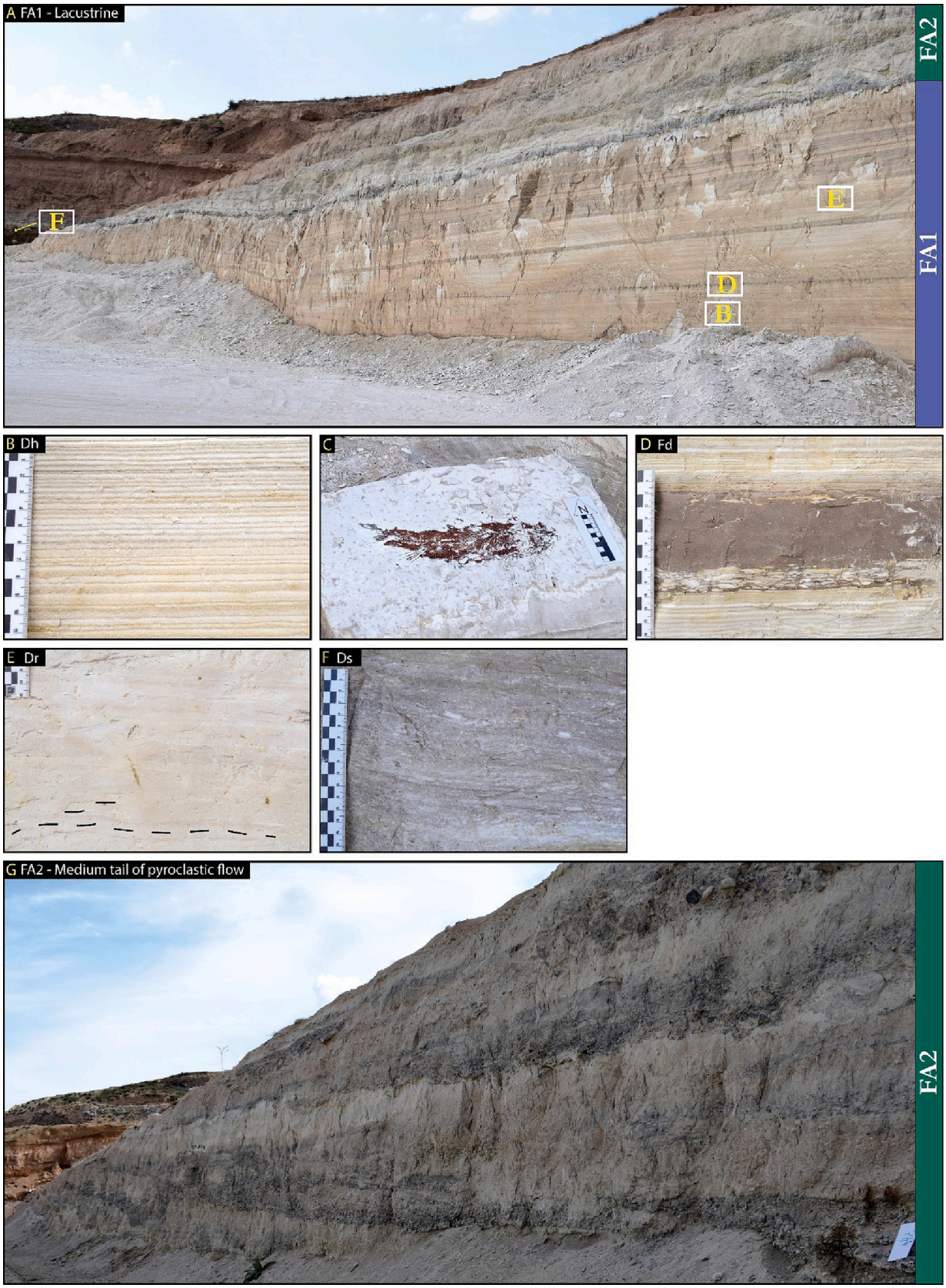

Fig. 3. 1. Lithological facies associations and facies recognised in the Jradzor section. Scale: hammer – 29.5 cm long, arrow – 15 cm long, black stick (Jacob's staff) – 1.5 m long. Description of facies as presented in pictures (B, D, E, F, I, O, P, T, U, V, X, A2) are summarised in Table 1. A. General view on lacustrine diatomite deposits present between 1.3 and 11 m; C. Fossil finding of *Capoeta* sp. fish at 5.7 m; G. General view on FA2 between 19 and 29 m; 2. H. Central part of the U-shaped incision in the FA2 with highly irregular basal surface; J. View on the wings of the U-shaped incision of the FA2; K. Expression of the pyroclastic surge with stratified volcanic tephra being cut by welded breccia of U-shape incision, 23.5 m; L. Fossil finding of tortois *Testudo* sp. in pedogenically modified ash-cloud surge deposits (JZ-

4, 24.45 m); M. Breccia Incisions in the FA3; N. Incision filled with normally-graded lapilli breccia, 52 m; Q. Horizon with carbonate nodule in FA3, 35 m; R and S. General views on palaeosol deposits, 42–45 m and 50–55 m respectively; 3. W. General view on the hummocky-shaped Gcg-breccia hill in the southern part of the quarry; Y. Alternation of poorly-sorted breccias with trough cross-laminated gravels in the northern (secondary) wall of the quarry interpreted as debris flow with periodic fluvial reworking; Z. Small scale incisions residing within the palaeosol horizons, 44 m; A1. General view on the lahar deposits, 46–51 m; A3. Lens with large mammalian fauna remains at the base of lahar deposits, 46 m.

to 7 m on the basin margins.

The FA3 contains sporadically distributed remains of land vertebrates, all located within the Fr-facies (See paragraph 4.4, Table 2). In the assemblages, the remains of small-sized vertebrates dominate, however, partial shells of tortoises and fragmented tusks of elephants are also found. The FA3 has less divers and fewer vertebrates remains than the FA2. The FA3 is typically succeeded by the FA4 (palaeosol) with gradational contact.

4.1.3.2. Interpretation. The FA3 is interpreted as representing distal tails of pyroclastic flows. The central part of the pyroclastic flow formed the Gcg-breccia by analogue with the FA2. The Smt-sandstones on the wings of incisions stand for a lighter fraction moving on the flow flanks with a relative delay compared to its central part. At the same time, the more fine-grained appearance of facies within the incision suggests that the area was subject to the most distal fine residue of the pyroclastic current.

The normal grading in the LTg-lapilli tuff that fills only one incision at 52 m represents a pumice flow (Fisher and Smith, 1991). The normal grading in pumice flow is not frequent but can be formed in more expanded pyroclastic flows where the pumice density was greater than the matrix (Cas and Wright, 1987). The incised appearance of the LTg-facies excludes an ash-fall origin.

Unlike topographically confined pyroclastic flows, the Fr-mudstones were initially deposited as an ash-cloud surge and had a wider mantling areal distribution. Consequently, the Fr-mudstone/tuff served as a ground for paedogenic processes. A decrease in the number, size and grain size of incisions and an increase in the size and abundance of rootlets and carbonate concretions in Fr-mudstone points at diminished pyroclastic flow-activity in the area and a moderate pedogenesis.

4.1.4. Facies association 4 (FA4) – palaeosols

4.1.4.1. Description. The FA4 has two distinct expressions (Fig. 3R, 3S). The first, up to 9 m thick packages are built of 0.2–1.3 m thick beds of reddish-brown mudstones (Fa) with mm- to cm-scale aggregates, mm- to cm-scale rootlets and numerous mm-scale dispersed fragments of volcanic rocks (pumice, lithics) (Fig. 3T). The contact between the beds is irregular, flame-like, with isolated rounded patches up to 10 cm in size. Locally, small lenses (30 × 10 cm) of poorly-sorted massive conglomerates (Gcm) occur among mudstones. The second expression of the FA4 is observed between 50.5 and 54.5 m. Here, reddish-brown mudstone (Fa) is penetrated by white meter-long rootlets that upward gradually pass into white crudely-stratified limestone (Fig. 3U). The limestone is followed by brown, aggregated claystone (C) with a sharp, irregular contact (Fig. 3S, 3V).

The FA4 is extremely poor on fossil remains. The only two fossiliferous horizons at 43.6 m (JZ-9) and at 36.75–37.2 m (JZ-9), residing within the Fa-facies, contain only one or two fossil taxa. The single bone find from JZ-9 shows bite marks.

The FA4 is succeeded by FA6 (Lahar) with an irregular contact or by the FA2 with sharp straight contact.

4.1.4.2. Interpretation. The FA4 is interpreted as palaeosols. The aggregate structure and rootlets of mudstone (Fa) and claystone (C) are indicative of active pedogenesis (Tabor et al., 2017). The rounded patches are krotovinas – the animal burrows of near sedimentation time that were later filled with mineral material (Pietsch, 2013; Ponomarenko and Ponomarenko, 2019). The rare lenses of conglomerates represent local small-scale rills (Fisher and Smith, 1991). The white limestone layer is interpreted as a calcrete – the soil horizon impregnated and cemented by paedogenic carbonate within fluctuating groundwater level (Zamanian et al., 2016). The brown aggregate claystone overlying the calcrete with sharp, irregular contact represents the illuvial clay horizon (Tabor et al., 2017). The presence of bite marks on the bone from the fossil horizon JZ-9 suggest exposure of the bone on the day-light surface and reworking by scavengers/predators.

The palaeosols are common in volcaniclastic records. Similar facies associations are known from the Late Pleistocene–Holocene volcanic record of the Lesser Antilles (Tate and Wilson, 1988) and the Holocene volcaniclastic record of the Vesuvius (Facies P sensu Sulpizio et al., 2006).

4.1.5. Facies association 5 (FA5) – debris flow/debris avalanche

4.1.5.1. Description. The FA5 is represented by poorly-sorted clast-supported pebble/cobble to boulder breccia (Gcm, Gcg) that appears in the section in different sizes and geometries. In the southern part of the quarry, the Gcg-breccia constitutes visually an up-to-35-m high and up-to-120-m broad hummocky-shaped hill, whose northern margin gently deepens towards the basin centre, where it is covered by diatomite (Fig. 3W). Both the matrix and clasts of the Gcg-facies have the same dacitic content, and the clasts are angular with sizes varying from millimetres to 1 m (Fig. 3X).

In the northern wall (correlates to 15–20 m in the western (main) wall, Fig. 2), within a remarkable 5-m-thick coarse-grained package, the extensive beds and lenses of poorly-sorted Gcg breccia with monogenetic dacitic clasts (1 cm to 0.6 m) alternate with up to 0.5-m-thick beds of parallel-laminated to trough cross-laminated moderately sorted granule gravel (Gct) (Fig. 3Y). The Gcg-facies has irregular but rather straight bases, while the Gct-facies demonstrates an irregular basal surface that makes scours into the Gcg-facies.

Smaller-scale up to 0.4 m thick and 5 m wide Gcm-lenses occur within the FA4, between 36.4 and 45 m. Here, the pebbles are subrounded to rounded (categories 3 and 4 according to Tucker, 2012) and have heterogeneous lithological content (Fig. 3Z).

The FA5 has no palaeontological remains detected. The FA5 forms the base of the section and occurs inbound with the FA2 and within the FA4.

4.1.5.2. Interpretation. The FA5 is interpreted as debris flows – fluid-saturated cohesive flows that deposit massive and matrix-supported sediments *en masse* as the shear stress falls below the yield strength of the flowing debris (Fisher and Smith, 1991; Smith, 1986).

The debris-prone hill on the southern part of the quarry that forms the base of the section is a product of the *debris avalanche* – a massive debris flow caused by the collapse of the volcanic edifice (Cas and Wright, 1987). As a characteristic feature, such avalanches form large-sized hills (from a few meters to 200 m high and more than 100 m in lateral extent) and are built of the lithic material of the volcano (Reading, 1996; Siebert, 1984). The occurrence of debris flow beds within the pyroclastic flow deposits results from remobilisation of the lose pyroclastic material during the interflow intervals and its transportation further downslope (Fisher and Smith, 1991).

The alternation of poorly-sorted breccias with trough cross-laminated gravels in the northern (secondary) wall represents episodic debris flows (Gcg) that were post-sedimentary affected by fluvial reworking.

The lenses of poorly-sorted breccia with subrounded pebbles between palaeosols formed as small-scale debris flow within rills. The

Fig. 3. (*continued*).

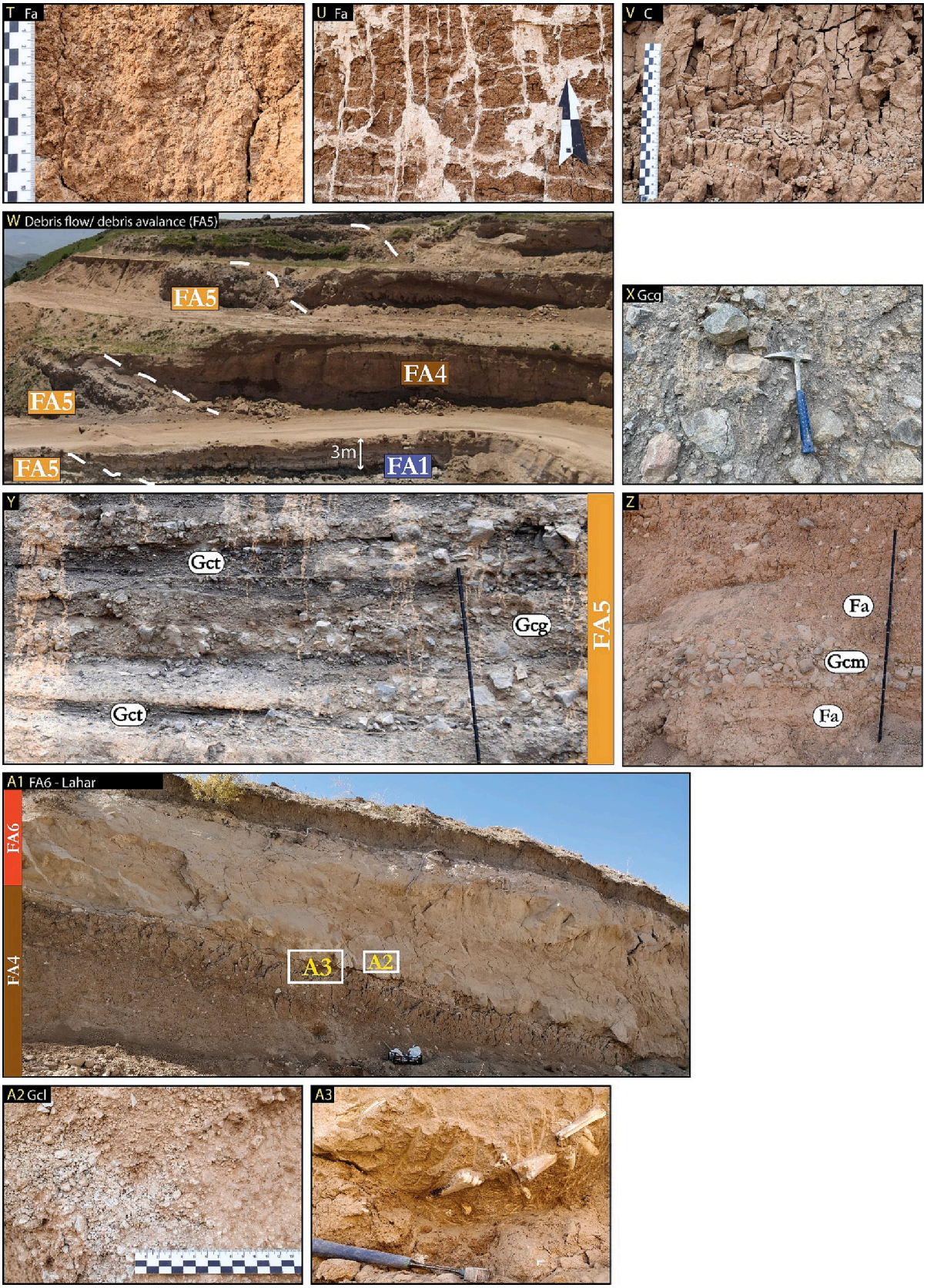

Fig. 3. (*continued*).

Table 2
Fossil horizons with their stratigraphic position in the section, interpreted palaeoenvironment, age ranges and faunistic composition. The age ranges were calculated through combination of $^{40}Ar/^{39}Ar$ data and magnetostratigraphic correlation to GPTS.

Fossil horizon	Strat. level	Palaeoenvironment (Facies association)	Age (Ma)	Nr of taxa	Taxonomic content
JZ-7	45.3–46.1 m	FA6 – Lahar	3.3 ± 0.03 Ma	13	*Bufotes* sp., Cricetinae indet., *Mimomys* cf. *davakosi,* Spalacinae indet., *Chasmaporthetes lunensis, Pliocrocuta perrieri, Miohyaenotherium* sp., *Nyctereutes* sp., *Hipparion* cf. *fissurae,* Antilopini indet. (cf. *Gazellospira*), Caprinae indet. (two species), Pliohyracinae indet.
JZ-9	43.6 m	FA4 – Palaeosol	3.6–3.33 Ma	1	Mammalia indet.
JZ-8	36.75–37.2 m	FA4 – Palaeosol	3.93 ± 0.05 Ma	3	Spalacinae indet., Ruminantia indet.
JZ-6	35–36.15 m	FA3 – Distal tail of pyroclastic flow	~4.16–3.98 Ma	21	*Bufotes* sp., Lacertidae indet., *Testudo* sp., Aves indet., *Talpa* cf. *fossilis*, Soricinae indet., *Ochotona antiqua*, *Ochotona* sp., Sciurinae indet., Glirinae indet., *Neocricetodon* sp., *Mesocricetus* cf. *primitivus*, *Cricetinae* indet., *Promimomys* sp., *Mimomys* cf. *davakosi*, *Mimomys* sp., *Apodemus* sp., *Pseudomeriones* cf. *tchaltensis*, *Pliospalax* cf. *macovei*, Cervidae indet. (cf. *Avernoceros*), Rhinocerotoidea indet., Proboscidea indet.
JZ-5a	30 m	FA3 – Distal tail of pyroclastic flow	~4.16–3.98 Ma	1	*Hipparion* cf. *fissurae*
JZ-5	29.3	FA3 – Distal tail of pyroclastic flow	~4.16–3.98 Ma	2	Testudines indet., Ochotonidae indet.
JZ-12	26.4–26.6 m	FA2 – Medium tail of pyroclastic flow	~4.16–3.98 Ma	1	*Hipparion* cf. *fissurae*
JZ-13 g	25.72–6.25 m	FA2 – Medium tail of pyroclastic flow	~4.16–3.98 Ma	1	Rodentia indet.
JZ-13	25.25–25.75 m	FA2 – Medium tail of pyroclastic flow	~4.16–3.98 Ma	24	*Bufotes* sp., *Hyla* sp., Agamidae indet., *Pseudopus* sp., Colubrinae indet. 1 (large-sized), Colubrinae indet. 2 (middle-sized), Colubrinae indet. 3 (small-sized), *Testudo* sp., Aves indet., *Talpa* cf. *fossilis*, *Asoriculus* cf. *gibberodon*, *Ochotona antiqua*, *Ochotona* sp., Leporidae indet., *Pliopetaurista* sp., *Neocricetodon* sp., *Promimomys* sp., *Mimomys* cf. *davakosi*, *Mimomys* sp., *Apodemus* sp., *Occitanomys* sp., *Pseudomeriones* cf. *tchaltensis*, *Pliospalax* cf. *macovei*, Mustelidae indet.
JZ-15	24.7–25.25 m	FA2 – Medium tail of pyroclastic flow	~4.16–3.98 Ma	2	Aves indet., *Deinsdorfia* sp.
JZ-14	24.45 m	FA2 – Medium tail of pyroclastic flow	~4.16–3.98 Ma	1	*Testudo* sp.
JZ-3s	23.45–24.35 m	FA2 – Medium tail of pyroclastic flow	~4.16–3.98 Ma	18	*Pelophylax* sp., Lacertilia indet., Colubrinae indet. 1 (large-sized), Colubrinae indet. 3 (small-sized), *Testudo* sp., Geoemydidae ident., Aves indet., *Talpa* cf. *fossilis, Asoriculus* cf. *gibberodon*, *Deinsdorfia* sp., *Ochotona antiqua*, *Ochotona* sp., *Neocricetodon* sp., *Mimomys* sp., *Apodemus* sp., *Pliospalax* cf. *macovei*, *Puma* sp., Caprinae indet.
JZ-3v	23.4 m	FA2 – Medium tail of pyroclastic flow	~4.16–3.98 Ma	5	*Testudo* sp., Serpentes indet., *Ochotona antiqua*, *Ochotona* sp., *Hipparion* cf. *fissurae*
JZ-3	22.75–23.3 m	FA2 – Medium tail of pyroclastic flow	~4.16–3.98 Ma	21	*Bufotes* sp., Lacertidae indet., *Varanus* sp., *Pseudopus* sp., Colubrinae indet. 2 (middle size), *Testudo* sp., Aves indet., *Asoriculus* cf. *gibberodon*, *Ochotona antiqua*, *Ochotona* sp., *Ochotonoma* sp., *Myomimus* cf. *maritsensis*, *Mesocricetus* cf. *primitivus*, *Neocricetodon* sp., *Promimomys* sp., *Mimomys* sp., *Apodemus* sp., *Occitanomys* sp., *Pseudomeriones* cf. *tchaltensis*, *Pliospalax* cf. *macovi,* Cervidae indet. (cf. *Arvernoceros*)
JZ-11	22.25 m	FA2 – Medium tail of pyroclastic flow	~4.16–3.98 Ma	2	*Testudo* sp., Antilopini indet. (cf. *Gazellospira*), Proboscidea indet.
JZ-11g	20.6–21.15 m	FA2 – Medium tail of pyroclastic flow	~4.16–3.98 Ma	1	Rodentia indet.
JZ-2a	19.8 m	FA2 – Medium tail of pyroclastic flow	~4.16–3.98 Ma	3	*Testudo* sp., Aves indet., Bovinae indet.
JZ-2	19.5 m	FA2 – Medium tail of pyroclastic flow	~4.16–3.98 Ma	3	*Testudo* sp., *Trischizolagus* cf. *dumitrescuae*, *Ochotona* sp.
JZ-1	1.3–12.3 m	FA1 – Lacustrine	~4.3 Ma	8	*Capoeta* sp., *Leuciscus* cf. *souffia, Leuciscus* sp., *Garra* sp., *Pelophylax* cf. *ridibundus,* Geoemydidae indet., Lagomorpha indet., Soricinae indet.

roundness of pebbles may point to an earlier reworking by colluvial/alluvial processes (Fisher and Smith, 1991).

4.1.6. Facies association 6 (FA6) – lahar

4.1.6.1. Description. The FA6 is represented by an up to 4.5 m-thick package of poorly-sorted clast- to matrix-supported lappili breccia (Gcl) with an intermittent 0.3 m-thick bed of brown rootled mudstone in the middle (Fr) (Fig. 3A1). The breccia consists of 2–10 mm white pumice fragments with a highly unequal distribution in the layer (Fig. 3A2). Locally, the Gcl is preceded by a 0.3 m-thick layer of grey massive fine-grained tuff (Tm). The FA4 delimits the FA6 with irregular upper and lower contacts.

The FA6 contains rich large mammalian fauna and rare remains of rodents and toads (fossil horizon JZ-7) concentrated in two lenses in the lowermost part of the package (Fig. 3. A1, A3). In the lenses, bones of different large mammalian taxa are sorted chaotically. A few of them belong to single individuals of different taxa (i.e., *Chasmaporthetes lunensis, Nyctereutes* sp., *Hipparion* cf. *fissurae*) which could be demonstrated by the presence of articulations between several bones (see Chapter 4.4, Fig. 7zb). Those bones retained either in vivo articulation or were slightly dispatched. Laterally and between these two lenses, isolated bones and teeth of different preservation are sporadically found. Those remains are heavily mineralized (silicified), contrary to bones from the lenses.

4.1.6.2. Interpretation. The FA6 is interpreted as lahar – "a rapidly flowing mixture of rock debris and water, other than normal streamflow, from a volcano" (Smith, 1986). The lahars are broadly considered as a type of volcanic debris flow with an increased clay/mud matrix induced by watering (through floods and rains) of unconsolidated pyroclastic debris (Suthren, 1985).

Chaotic distribution of pumice fragments within a muddy matrix points at a high depositional energy of the flow. The lack of lithics and prevalence of pumice in the FA6 may suggest that only the distal and the lightest fraction of the flow was accumulated in the area. On the other

hand, the prevalence of pumice and a one-bed appearance of the FA6 may indicate that the lahar resulted from one pyroclastic fall event whose products were rapidly remobilised downslope. The layer of grey tuff at the base represents a basal flow layer formed by shearing (Suthren, 1985).

The chaotic distribution of various large vertebrate remains of the JZ-7 fossil horizon within the lahar also supports a conclusion about a rapid and high-energy character of the mudflow. Accumulation of the bones at the base of the flow may indicate the relatively high water-saturation of the flow (i.e. the bones were denser than the mudflow). The concentration of numerous large and small vertebrate taxa in two lenses suggests that the animal bodies were probably washed into small palaeotopographic depressions or pockets. At the same time, partial articulation of a number of fragments and closely located bones of single individuals (e.g. both mandibles and skull of *Nyctereutes* are found in a distance of around 10 cm, partially articulated hindlimb of *Hipparion* cf. *fissurae*) and lack of corrosion on the bone surfaces point at a relatively small transportation distance from the drowning place.

Lahars are typical depositional deposits within volcanic regions, especially those rich in lose pyroclastic deposits. The FA6 in Jradzor is similar to pumice-rich lahars of the Colima stratovolcano in Mexico (Rodríguez-Sedano et al., 2022) as well as have some textural similarities with "grey and black pumice lahar" of the Changbaishan Tianchi stratovolcano in China (Yi et al., 2019).

4.2. Magnetostratigraphy

Demagnetisation of 71 samples showed a presence of two magnetic components. The first one is a low temperature/low field component that demagnetises in a range 20–180 °C or 0–20 mT (Fig. 4A, B). The mean directions for both the AF- and TH-samples calculated with α95 confidence limits are nearly identical on the areal plots and thus were combined into one statistic group "1st component". The parameters of the "1st component" mean direction are: D = 3.94°, *I* = 51.21°, k = 18,72, α95 = 5.23 for *N* = 42 in geographic coordinates (Fig. 4C). The first component is usually associated with either a current day magnetic overprint or stands for a viscous remanent magnetisation. On the date of the last sampling (May 25, 2021), the magnetic field in the Jradzor area had parameters of *I* = 59.12° and D = 6.22° (ngdc.noaa.gov). The acquired inclination of the "1st component" is about 8° shallower than that of the local magnetic field. A wide spread of magnetic directions on the area plot may point at the significant role of viscous magnetisation in building the "1st component". We interpreted the 1st magnetic component as a mixture of the current-day magnetic overprint and viscous remanent magnetisation.

The second magnetic component is typically demagnetised in range 480–580 °C or 60–80 mT (Fig. 4A, B). Thermomagnetic runs resulted in a gradually decreasing reversible demagnetisation curve that eventually drops off at 580 °C (Fig. 4D). Such behaviour is characteristic for magnetite (Mullender et al., 1993), which is, thus, considered to be the primary magnetic carrier in the Jradzor samples.

The second component comprises directions with negative and positive inclination values and, thus, was split into two statistical groups, "2nd reversed" and "2nd normal" respectively (Fig. 4E). The "2nd reversed" group combines directions from both AF- and TH-demagnetised samples and has the following parameters of the mean direction: D = 166°, I = -46.1°, k = 13.53, α95 = 5.94 for *N* = 46 in tectonic coordinates (Fig. 4E). The mean direction for the "2nd normal" group has parameters of D = 330.3°, *I* = 35.1°, k = 6.55, α95 = 28.3 for *N* = 6 in tectonic coordinates. Such a small number of samples makes this mean direction unreliable and further statistical analysis impossible.

The expected inclination for the latitude 40°01′ of the Jradzor section is *I* = 59.2° according to the geocentric axial dipole (GAD). The inclination I = -46.1° of the "2nd reversed" group is much shallower than expected. We used the elongation/inclination (E/I) test of Tauxe and Kent (2004) that fits observed inclinations to the TK03 to test the probable inclination shallowing. GAD Field Model using the flattening function of King (1955). The bootstrap test used in the E/I method shows an average unflattened mean inclination of −52.48° with the bootstrapped confidence interval between −67° and − 44° (Fig. 4F). Therefore, the E/I method revealed a ~ 6.4° inclination shallowing. However, the more precise assessment of the inclination shallowing would require more samples as the number of measured samples is only 50 against 80 recommended. The second magnetic component is a distinct pre-tilt component characterised by high temperature/high field demagnetisation and carried by magnetite. We interpret the second magnetic component as characteristic remanent magnetisation (ChRM).

Plotting the ChRM directions in stratigraphic order discloses four reversed polarity intervals: R1 (0–26,8 m), R2 (36.9–43.1 m), R3 (45.4–50 m), R4 (52.2–55.6 m); two small normal polarity intervals: N1 (43.1–44 m) followed by a small interval with uncertain polarity and N2 (50–52.2 m) (Fig. 5). Across the section, there are also five single samples with normal polarity occurring within stable series of reversed samples. Due to the small number of normal polarity samples, it was impossible to apply the α95 cut-off. Hence, some of these outliers may represent either local anomalies or be statistically rejected samples.

4.3. $^{40}Ar/^{39}Ar$ chronology

For JZ-V1, we analysed a feldspar fraction with 10 grains/hole per fusion. K/Ca ratios range between 1 and 2, and this is, therefore, not a pure sanidine fraction. Radiogenic ^{40}Ar yields range from 20% to 80%. Low radiogenic argon yields might suggest alteration and argon loss, and, therefore, yield ages that are too young. However, we do not observe a correlation between (low) $^{40}Ar^*$ and (young) age, and therefore assume that alteration does not play a major role, although we cannot completely exclude this. Ages range from 3.7 to 6.3 Ma. If we select the weighted mean age according to our approach I based on the youngest age population including analyses with overlapping ages with MSWD < *t*-test statistic at 95% confidence level, the weighted mean age arrives at 4.29 ± 0.09 Ma (4 out of 10 analyses). The atmospheric $^{40}Ar/^{36}Ar$ inverse isochron intercept is 300.7 ± 6.8 (Fig. 6). An alternative approach II includes the highest number of analyses with overlapping ages and MSWD < t-test statistic at 95% confidence and level yields 4.52 ± 0.08 Ma (5 out of 10 analyses). Assuming the youngest age populations are approaching eruption ages and because of potential older grains can be present in multigrain experiments, we use these in our stratigraphic framework.

For JZ-V2 we analysed a feldspar fraction with 10 grains/hole per fusion. K/Ca ratios are ~0.3. Radiogenic ^{40}Ar yields range from 12% to 74%. Ages range from 3.8 to 4.8 Ma. The weighted mean age arrives at 4.05 ± 0.11 Ma (6 out of 10 analyses) according to approach I. The atmospheric $^{40}Ar/^{36}Ar$ inverse isochron intercept is 297.9 ± 5.6 (Fig. 6). Approach II includes a similar number of analyses yielding 4.23 ± 0.08 Ma (6 out of 10 analyses). Also here, we assume that the youngest age populations are approaching eruption ages, which are used in our stratigraphic framework.

For JZ-V3, we analysed a feldspar fraction with 10 grains/hole per fusion. K/Ca ratios are ~0.5. Radiogenic ^{40}Ar yields range from 13% to 69%. Ages range from 4.0 to 15.3 Ma. Approach I and II both yield a weighted mean age of 4.07 ± 0.09 Ma (3 out of 10 analyses). The atmospheric $^{40}Ar/^{36}Ar$ inverse isochron intercept is 298.4 ± 6.1 (Fig. 6).

For JZ-V4, we analysed the sanidine fraction with 10 grains/hole per fusion. K/Ca ratios range between 0.8 and 2.3, and this is, therefore, not a pure sanidine fraction. Radiogenic ^{40}Ar yields range from 24% to 83%. Ages range from 3.8 to 4.1 Ma. If we select the weighted mean age based on the youngest population, including the highest number of analyses with overlapping ages and MSWD < *t*-test statistic at 95% confidence level (approach I), the weighted mean age arrives at 3.93 ± 0.05 Ma (6 out of 10 analyses). The atmospheric $^{40}Ar/^{36}Ar$ inverse isochron intercept is 298.1 ± 4.9 (Fig. 6). Approach IIarrives at 3.99 ± 0.04 Ma (7 out of 10 analyses).

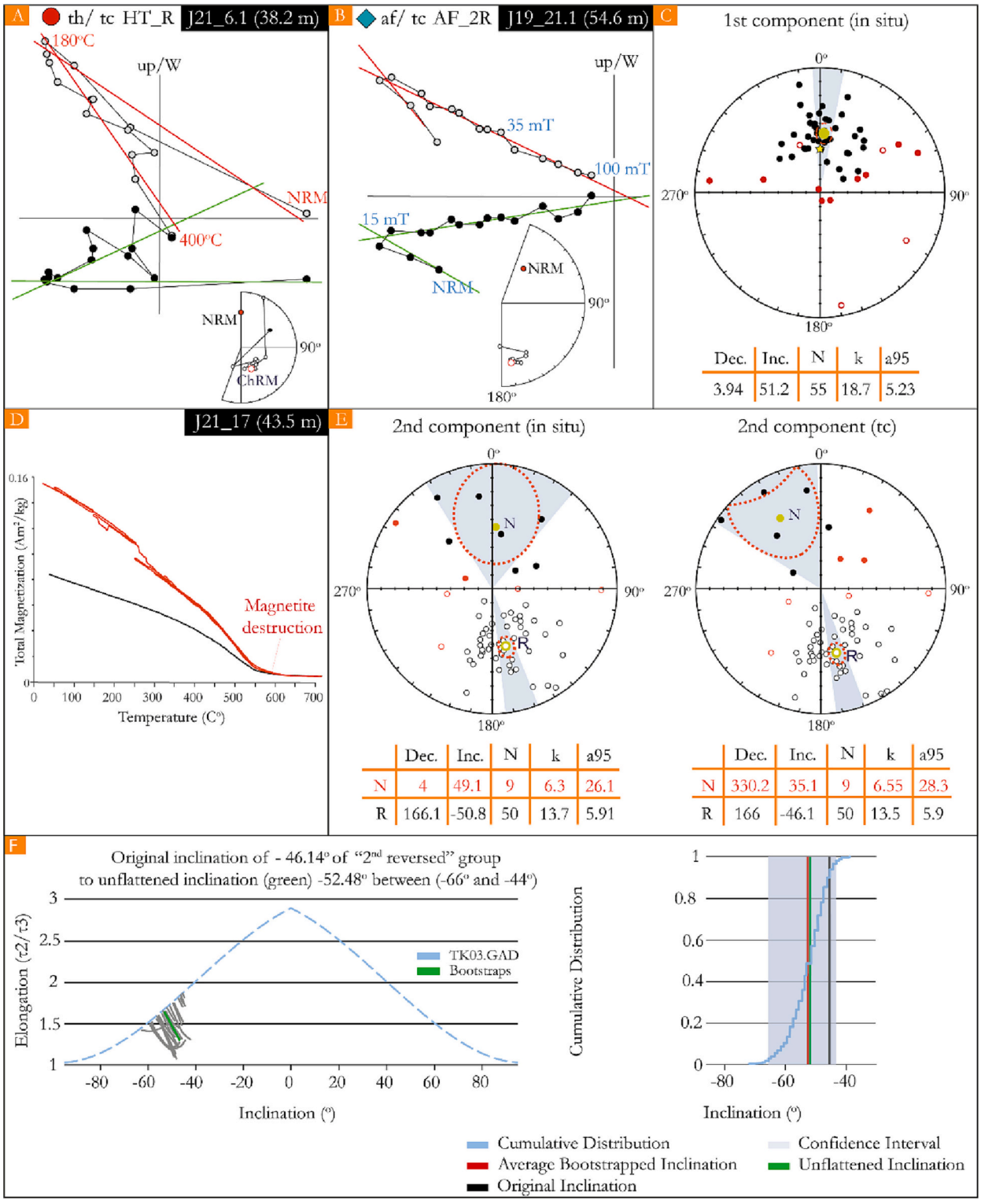

Fig. 4. Zijderveld diagrams, equal area plots, and thermomagnetic curves of palaeomagnetic samples from the Jradzor section. Zijderveld diagrams: A and B – for reversed samples. Equal are plots of the: C. Low-intensity 1st component; E. "2nd component" (combined high temperature and high-intensity components for all reversed and all normal samples); D. Thermomagnetic run curves with magnetite being interpreted as the main magnetic carrier. F. Bootstrap test curve showing the inclination shallowing in "2nd reversed" group; Abbreviations: in situ – geographic coordinates; tc – tectonically corrected coordinates, NRM – Natural remanent magnetisation, ChRM – Characteristic remanent magnetisation, Dec. – declination, Inc. – inclination, N – number of statistically accepted samples, k – precision parameter of Fisher (1953), α95–95% cone of confidence.

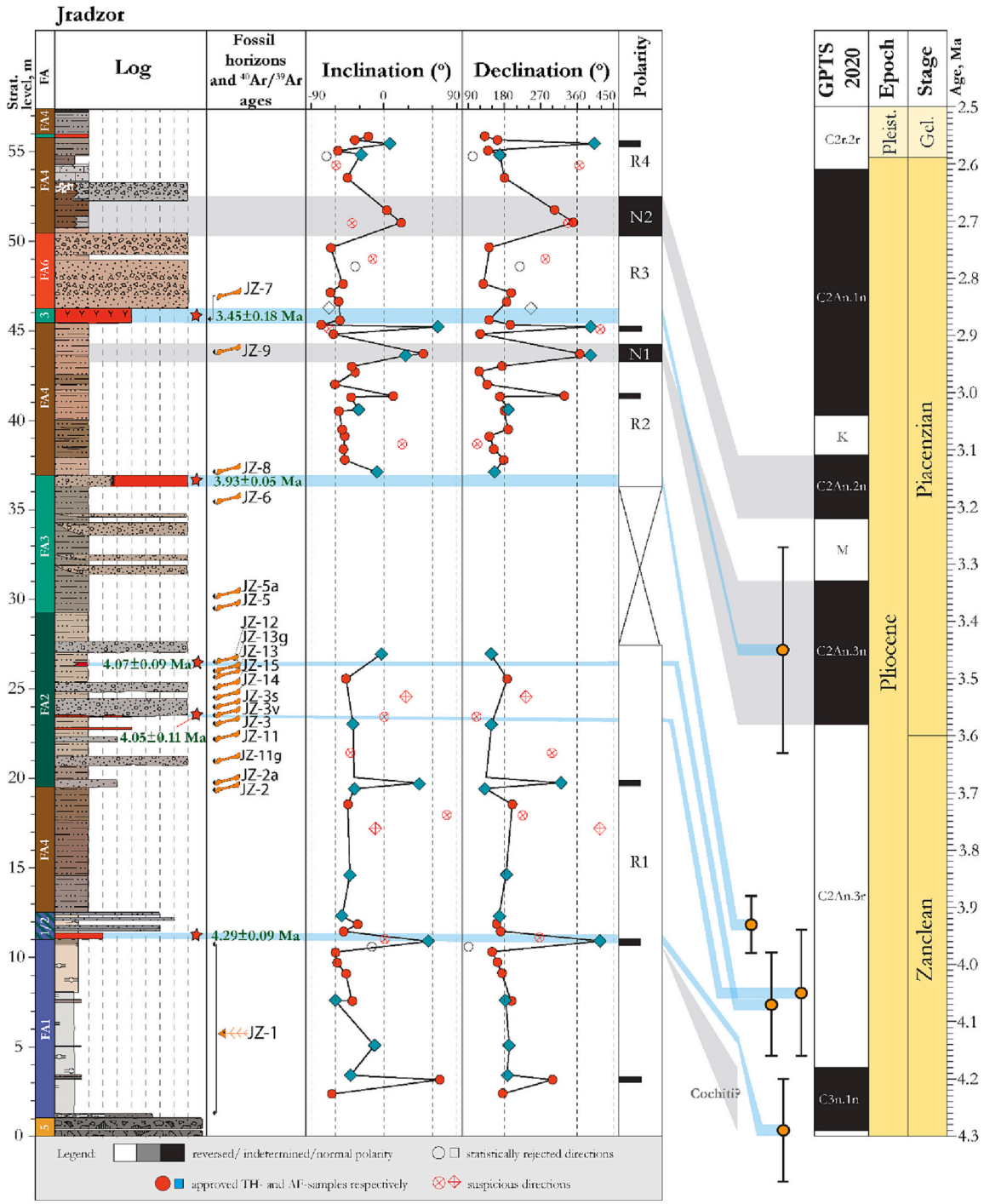

Fig. 5. Magnetostratigraphy, $^{40}Ar/^{39}Ar$ dates and fossil horizons of the Jradzor section and their correlation to GPTS. FA – facies association, for the codes, see Fig. 2.

For JZ-V5 we analysed both single grains and ~ 5–10 grains/hole per fusion. The single grain analyses yield too low signals to be reliably measured. The 15 experiments on 5–10 grains/sample still yield a too-low signal for $n = 5$. The remainder shows an age distribution ranging from 2.5 to 13.5 Ma. The samples with radiogenic ^{40}Ar yields >10% yield a weighted mean age of 3.45 ± 0.18 Ma following approach I. Although errors are relatively large, this age is in correct stratigraphic order.

4.4. Palaeontology and fossil horizons

In total, 19 fossiliferous horizons with at least 48 vertebrate taxa (excluding birds) were identified in the 57-m-thick succession. They include four fish, three amphibian (only frogs), nine reptilian and 30 mammalian taxa (Supplementary 5). Preliminary observations on the avian fauna suggest the presence of several taxa (pers. communication of Dr. Gerald Mayr), whose taxonomic identification, however, will be studied in detail elsewhere.

The fossiliferous horizons have different richness. The richest horizons are the JZ-3, JZ-3s, JZ-13 and JZ-6. Here, the number of taxa varies between 18 and 24 taxa. The highest concentration of the fossiliferous horizons is confined to the package between 19.5 and 27 m, which belongs to the FA2 – medium tail of pyroclastic flows. The fewer taxa (<5) have been found in the horizons JZ-2, JZ-2a, JZ-11g, JZ-11, JZ-3v, JZ-

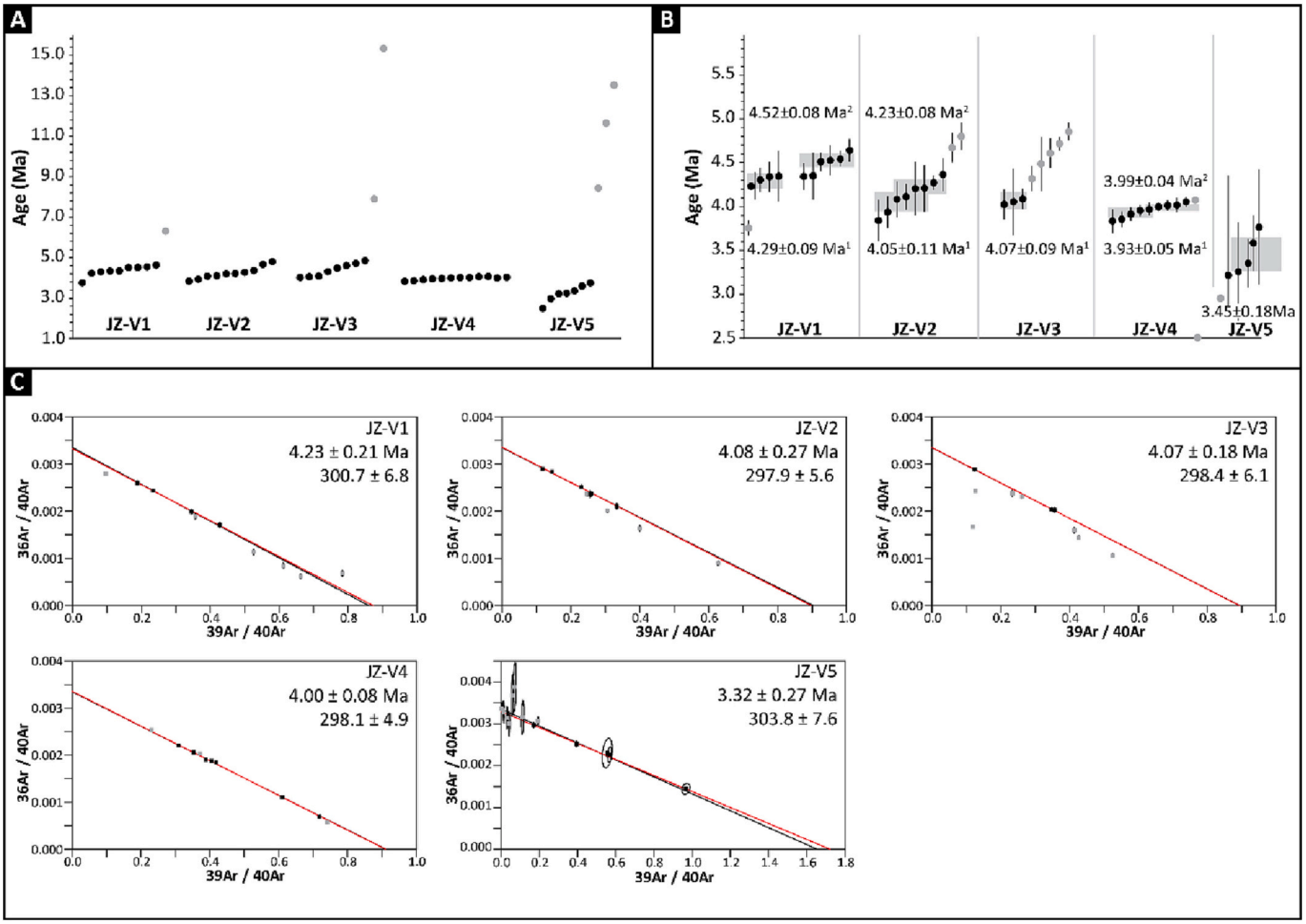

Fig. 6. Summary of $^{40}Ar/^{39}Ar$ ages. A. All individual analyses with their 2σ analytical uncertainty (mostly smaller than symbol size); B. individual analyses with their 2σ analytical uncertainty in the 3.5–5.0 Ma range. Grey rectangles and different ages indicate different interpretations for the eruption age (see text) according to two approcahes: 1. Youngest age population: data points included until MSWD > t-test statistic at 95% confidence level; 2. Highest number of data points included until MSWD > t-test statistic at 95% confidence level; C. Inverse isochrones of JZ-V1, JZ-V2, JZ-V3, JZ-V4 and JZ-V5. The red line represents the inverse isochron line. The black line is the reference line. Black (grey) squares are included (excluded) in isochron age. 2σ error ellipses are shown but are often smaller than the symbol size of data points. (For interpretation of the references to colour in this figure legend, the reader is referred to the web version of this article)

14, JZ-15, JZ-13g, JZ-12, JZ-5, JZ-5a, JZ-8, JZ-9. An intermediate richness has been documented in JZ-1 (8 taxa) and JZ-7 (13 taxa).

The lowermost fossil horizon JZ-1 (1.3–12.3 m), only situated in the lacustrine diatomite deposits (FA1), comprises nearly exclusively aquatic forms (fishes, frog, turtle) (the only rabbit remain is transported from the land) (Fig. 7). The other fossil horizons contain diverse land forms except for the JZ-3s (23.45–24.35 m), which also include partially aquatic forms (*Pelophylax* sp., Geoemydidae indet.). The most common elements in fossil assemblages across all fossiliferous horizons are the tortoises (*Testudo* sp.) and pikas (*Ochotona* sp./Ochotonidae indet.) (Fig. 7, Table 2, suppl table 5. Besides JZ-7, all fossiliferous horizons from terrestrial settings (i.e., excluding JZ-1) contain small-sized vertebrate remains (bones/teeth). In contrast, the JZ-7 is the only horizon with well-preserved remains of large-sized vertebrates (large mammals), where the best-preserved bone reaches a length of up to 36 cm.

5. Discussion

5.1. Correlation to geological time scale (GTS)

5.1.1. Magnetostratigraphic and $^{40}Ar/^{39}Ar$ correlation to GTS

The combination of $^{40}Ar/^{39}Ar$ dating, magnetostratigraphy and biochronology provides with a high-resolution chronostratigraphic framework for the Jradzor section and enables the important tying point for the Eurasian palaeobiogeography.

The five volcanic tephras dated with $^{40}Ar/^{39}Ar$ method provided ages ranging from 4.29 ± 0.09 Ma to 3.45 ± 0.18 Ma (Fig. 6). The two lowermost tephras – JZ-V1 (11 m) and JZ-V2 (23.4 m) comprise ages of 4.52 ± 0.08 Ma and 4.29 ± 0.09 Ma for the JZ-V1 and 4.23 ± 0.08 Ma and 4.05 ± 0.11 Ma for the JZ-V2 depending on statistical approach (Fig. 5). Both tephras represent parts of pyroclastic density currents – pyroclastic flow (JZ-V1) and pyroclastic surge (JZ-V2), respectively. The pyroclastic flows and surges are gravitation-controlled currents with high erosional capacity that tend to occupy the lowermost topographies (Cas and Wright, 1987). The newly approaching pyroclastic flows and surges onlap on top of pyroclastic deposits of the previous flows/surges. Each new pyroclastic current eventually creates a mixture of true volcaniclastic and epiclastic components. The presence of two age populations in the JZ-V1 and JZ-V2 may point to such a mixture, where the oldest age indicates the previously deposited and reworked pyroclastic deposits (epiclastic component), and the youngest age represents the new pyroclastic flow (true volcaniclastic component). In this case, the youngest age approaches the true sedimentation age, while the oldest age may indirectly indicate the presence of older pyroclastic density currents developed upslope.

The JZ-3V sample (26.7 m) has an age of 4.07 ± 0.09 Ma, which is

(caption on next page)

Fig. 7. Fossil material from the Jradzor section. a) Skeleton of *Capoeta* sp. (JRD-17/07, JZ-1), b) partial skeleton of *Pelophylax* sp. (GLS-07/6, JZ-1), c) epiplastron of Geoemydidae indet. (ventral view) (JRD-13/133, JZ-1), d) scapula of *Bufotes* sp. (ventral view) (JRD-18/33, JZ-3), e) ilium of *Hyla* sp. (lateral view, JRD-19/102, JZ-13), f) maxilla of Agamidae indet. (labial view) (JRD-19/116, JZ-13), g-h) vertebra of Colubrinae indet. (lateral [g] and dorsal [h] views) (JRD-18/20, JZ-3s), i) vertebra of Aves indet. (dorsal view) (JRD-18/15, JZ-3s), j) right humerus of *Talpa* cf. *fossilis* (distal view) (IGS unnumbered; JZ-13), k) left mandible with m1-m2 of *Asoriculus* cf. *gibberodon* (lingual, occlusal and articular views) (JRD-18/23, JZ-3s), l) left mandible with m1-of *Deinsdorfia* sp. (lingual, occlusal and articular views) (IGS unnumbered; JZ-15), m) right p3 of *Trischizolagus* cf. *dumitrescuae* (occlusal view) (JRD-17/02, JZ-2), n) right p3 of *Ochotona antiqua* (occlusal view) (IGS unnumbered, JZ-3), o) left p3 (invers) of *Ochotonoma* sp. (occlusal view) (IGS unnumbered, JZ-3), p) right mandible fragment with m2-m3 of *Pliopetaurista* sp. (lingual and occlusal views) (IGS unnumbered, JZ-13), q) right mandible with m1-m3 of *Pliospalax* cf. *macovei* (lingual and occlusal views) (IGS unnumbered, JZ-3), r) left lower m1 of Neocricetodon sp. (buccal and occlusal views) (IGS unnumbered, JZ-3), s) left mandible with m1-m2 (invers) of *Mesocricetus* cf. *primitivus* (buccal and occlusal views) (IGS unnumbered, JZ-3), t) right m1 (mirrored) of *Promimomys* sp. (buccal and occlusal views) (IGS unnumbered, JZ-3), u) left m1 of *Mimomys* cf. *davakosi* (buccal and occlusal views) (IGS unnumbered, JZ-3), v) left m3 of *Myomimus* cf. *maritsensis* (buccal and occlusal views) (IGS unnumbered, JZ-3), w) right mandible with m1-m2 (mirrored) of *Apodemus* sp. (buccal and occlusal views) (JRD-18/04, JZ-3s), x) left m1 of *Occitanomys* sp. (buccal and occlusal views) (IGS unnumbered, JZ-3), y) left m1 of *Pseudomeriones* cf. *tchaltensis* (buccal and occlusal views) (IGS unnumbered, JZ-13), z) right lower jaw of *Lynx* sp. with c1, p3, p4 (lateral view) (JRD-18/65, JZ-3s), za) skull of *Nyctereutes* sp. (lateral view) (JRD-20/03, JZ-7), zc) maxillae of Bovidae indet. (ventral view) (JRD-19/84 and – 20/19, JZ-7), zd) lower jaw of *Hipparion* cf. *fissurae* (occlusal view) (JRD-19/97, JZ-7), zb) tibia (JRD-17/29) in articulation with talus (JRD-17/28) and calcanaus (JRD-17/19) of *Hipparion* cf. *fissurae* (JZ-7).

slightly older but statistically overlaps with the underlying JZ-V2 (23.4 m, 4.05 ± 0.11 Ma). However, we still consider the JZ-3V reliable as both of these tephras have a close stratigraphic position and have an overlapping error range. The uppermost tephras JZ-V4 (36.2 m) and JZ-V5 (35.2 m) were accumulated from the ash-cloud surge – the dispersed residue of the pyroclastic flows. The JZ-V4 provides an age of 3.93 ± 0.03 Ma (approach I) or 3.99 ± 0.04 Ma (approach II), while the JZ-V5 has an age of 3.54 ± 0.18 Ma with a large analytical error. All $^{40}Ar/^{39}Ar$ ages show relatively low radiogenic ^{40}Ar yields (so a relatively high non-radiogenic ^{40}Ar component in the sample that is not the product of radioactive decay of ^{40}K but comes from other sources). If the proportion of ^{36}Ar is high and we assume that this is derived from a trapped atmospheric component, then the $^{40}Ar^*$ signal is diluted, and the radiogenic ^{40}Ar yield is lower. This will still result in reliable but lower precision ages (larger uncertainties). High atmospheric Ar abundances may result from incomplete degassing of the melt during eruption (when assuming an initial trapped argon component that is isotopically atmospheric, a reliable age can still be obtained) or the interaction of meteoric fluids with the minerals during eruption, cooling and/or hydration, leading to alteration. In addition, a low $^{40}Ar^*$ content can suggest argon loss, leading to younger ages. However, we do not observe a correlation between (low) $^{40}Ar^*$ and (young) age. We cannot distinguish between these different processes, but because the ages more or less follow that stratigraphic order, we assume that the minerals behave as a closed system with a trapped atmospheric component. To interpret this $^{40}Ar/^{39}Ar$ data set, integration with other methods, such as magnetostratigraphy, is crucial.

The magnetic polarity patterns of the Jradzor section consist of dominantly reversed polarity (zones R1, R2, R3 and R4) with two small normal polarity zones N1 (43.1–44 m) and N2 (50.1–52.4 m) located in the upper part of the section (Fig. 5). There are also six single normal polarity samples spread throughout the section (at 3.1, 10.8, 19.6, 41.15, 45 and 55.2 m) (Fig. 5).

Similar to the $^{40}Ar/^{39}Ar$ data, the magnetostratigraphic results also endured complications caused by specific depositional environments. The erosive nature of the pyroclastic density currents and intervening reposes between them, followed by the lack of sedimentation and/or different volumes of accumulated material, create numerous small-scale gaps disturbing the continuity of the record. Because of that, the magnetic zones may vary in their thickness.

Using the age constraints provided by the $^{40}Ar/^{39}Ar$ dating, we correlate the lower part of the reversed zone R1 (0–10.8 m) to the C3n.1r chron (Fig. 5). The single normal sample at 10.8 m, located just below sharp-based volcanic tephra JZ-V1 (11 m, 4.29 ± 0.09 Ma), may potentially represent the remnants of the C3n.1n (Cochiti) chron. However, this assumption remains highly speculative. Counting of varves in diatomite below the JZ-V1 tephra (Chapter 4.1.1) suggested the duration of the lacustrine phase between 2 and 3 ky implying that the base of the section cannot be much older than 4.3 Ma.

The upper part of the R1 and the R2 zones containing volcanic tephras with ages 4.07–3.99 Ma, we correlate to the C2An.3r chron (Fig. 5). The normal zone N1 marks the first stable change in magnetic polarity after a long reversed interval. We correlate the N1 zone to the lower Gauss subchron (C2an.3n). This correlation is generally supported by the stratigraphically higher volcanic tephra JZ-V5 which has an age of 3.45 ± 0.18 Ma. The following intervals R3, N2 and R4, we correlated to the chrons C2An.2r (Mammoth), C2An.2n (Middle Gauss) and C2An.1r (Kaena), respectively.

The single normal samples spread throughout the section may potentially be statistically unreliable or represent the local magnetic anomalies. Nevertheless, their statistical approval/discrimination was not feasible due to the extremely low number of samples with normal polarity. In conclusion, the integration of magnetostratigraphic, $^{40}Ar/^{39}Ar$ dating accompanied by sedimentological analysis show that the Jradzor section spans the time interval between ~4.3 and 3.03 Ma.

5.1.2. Biochronologic correlation to GTS

The biochronological ranges of the small mammalian taxa of the Jradzor section vary between MN12 to MN17 (Fig. 8). The taxa with broad stratigraphic coverage (MN12–15, and beyond) include *Asoriculus gibberodon* (Reumer, 1984; Rzebik-Kowalska, 1994; Vasileiadou and Doukas, 2022), *Ochotona antiqua* (Čermák, 2010; Erbajeva, 1994; Nesin, 2013), *Myomimus maritsensis* and *Mesocricetus primitivus* (Hordijk and de Bruijn, 2009; Vasileiadou and Sylvestrou, 2022b), and *Neocricetodon* (MN12–16) (Vasileiadou and Sylvestrou, 2022b). *Talpa fossilis*, the genera *Deinsdorfia* (Reumer, 1984; Rzebik-Kowalska, 1994; Vasileiadou and Doukas, 2022), *Pliopetaurista* (Colombero and Carnevale, 2016; Mein, 1970; Vasileiadou and Sylvestrou, 2022b), *Apodemus* and *Occitanomys* (Nesin, 2013; Nesin and Storch, 2004; Vasileiadou and Sylvestrou, 2022b) have the broadest range from the Late Miocene to Quaternary.

The species *Trischizolagus dumitrescuae* (Čermák et al., 2015), *Promimomys* (Dahlmann, 2001; Hordijk and de Bruijn, 2009; Vasileiadou and Sylvestrou, 2022b), *Mimomys davakosi* (Fejfar et al., 1998; Hordijk and de Bruijn, 2009; Vasileiadou and Sylvestrou, 2022b) and *Pliospalax macovei* (Sen and Sarica, 2011; Vasileiadou and Sylvestrou, 2022b) are known as MN14–15 taxa, whereas the species *Pseudomeriones tchaltensis* (Sen, 1977; Sylvestrou and Kostopoulos, 2007) and the genus *Ochotonoma* (Čermák, 2007; Sen, 1998) are restricted exclusively to MN15. *Pseudomeriones* and *Ochotonoma* have been found in the horizons JZ-3, JZ-13 and JZ-6. Among large mammalian taxa, *Hipparion* cf. *fissurae* (horizons JZ-3v, JZ-5a, JZ-7) is also limited to MN15 (Bernor et al., 1996; Cirilli et al., 2021; Zouhri and Bensalmia, 2005). The overlapping interval of all taxa from fossiliferous horizons can be unambiguously correlated to the MN15.

The only disagreement could be that *Mimomys* cf. *davakosi* is present

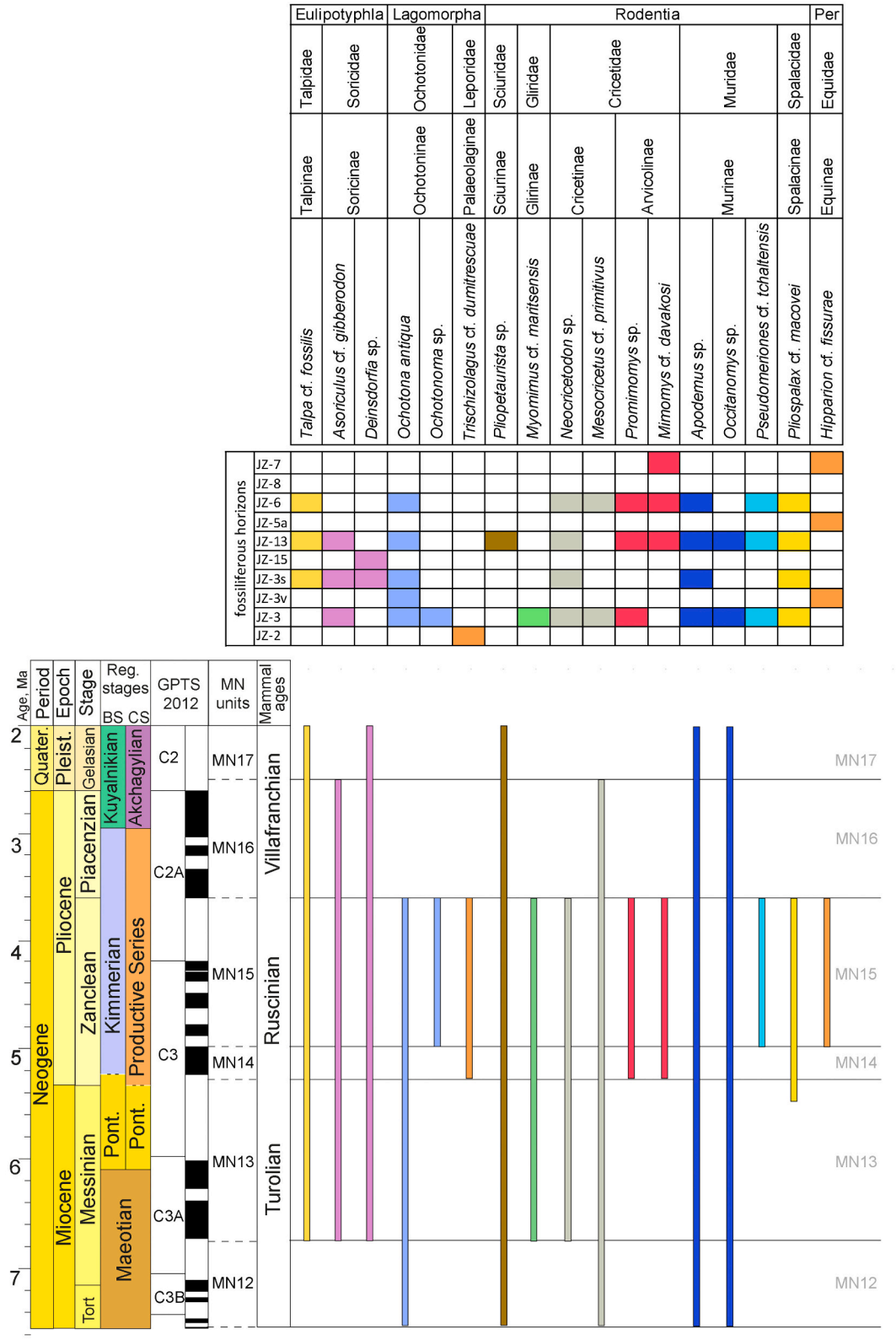

Fig. 8. Fossil record of the small and large mammals (relevant for the biochronologic correlation) from the fossiliferous horizons of the Jradzor section with indication of their biochronologic coverage along the MN-units according to the current knowledge. Note, the age limits of the MN-units follow that of Raffi et al. (2020). Abbreviation: Per - Perissodactyla.

in the uppermost fossiliferous layer JZ-7, for which an absolute age of 3.3 ± 0.03 Ma was determined. This age would already correspond to MN16 (a), which is the *Mimomys hassiacus* (=*hajnackensis*)-*Mimomys stehlini* zone sensu Fejfar et al. (1998) in Europe and in western Turkey (Skandalos et al., 2023). The occurrence of the *Mimomys* cf. *davakosi* in these younger deposits could be potentially linked to reworking if considering

the European stratigraphic occurrence of the taxon. However, as mentioned below, we interpret the fossiliferous layer JZ-7 as less probably to represent a redeposited material from older rocks. As solid arguments of the interpretation we consider: similar preservation of all the bones (e.g. colour, mineralisation degree); frequent anatomic (partial) articulation; close location of the bones of the same individuals of both large- (*Nyctereutes* sp., *Hipparion* cf. *fissurae*) and small-sized animals (*Bufotes* cf. *viridis*) in the sediment; lack of reworking traces and bone corrosion. Alternatively, the explanations could be that *M. davakosi* could either maintain longer in the Caucasus or that the Jradzor finds represent a transitional form between *M. davakosi* and *M. hajnackensis*, the separation (according to the occlusal surface, the crown height, and height of

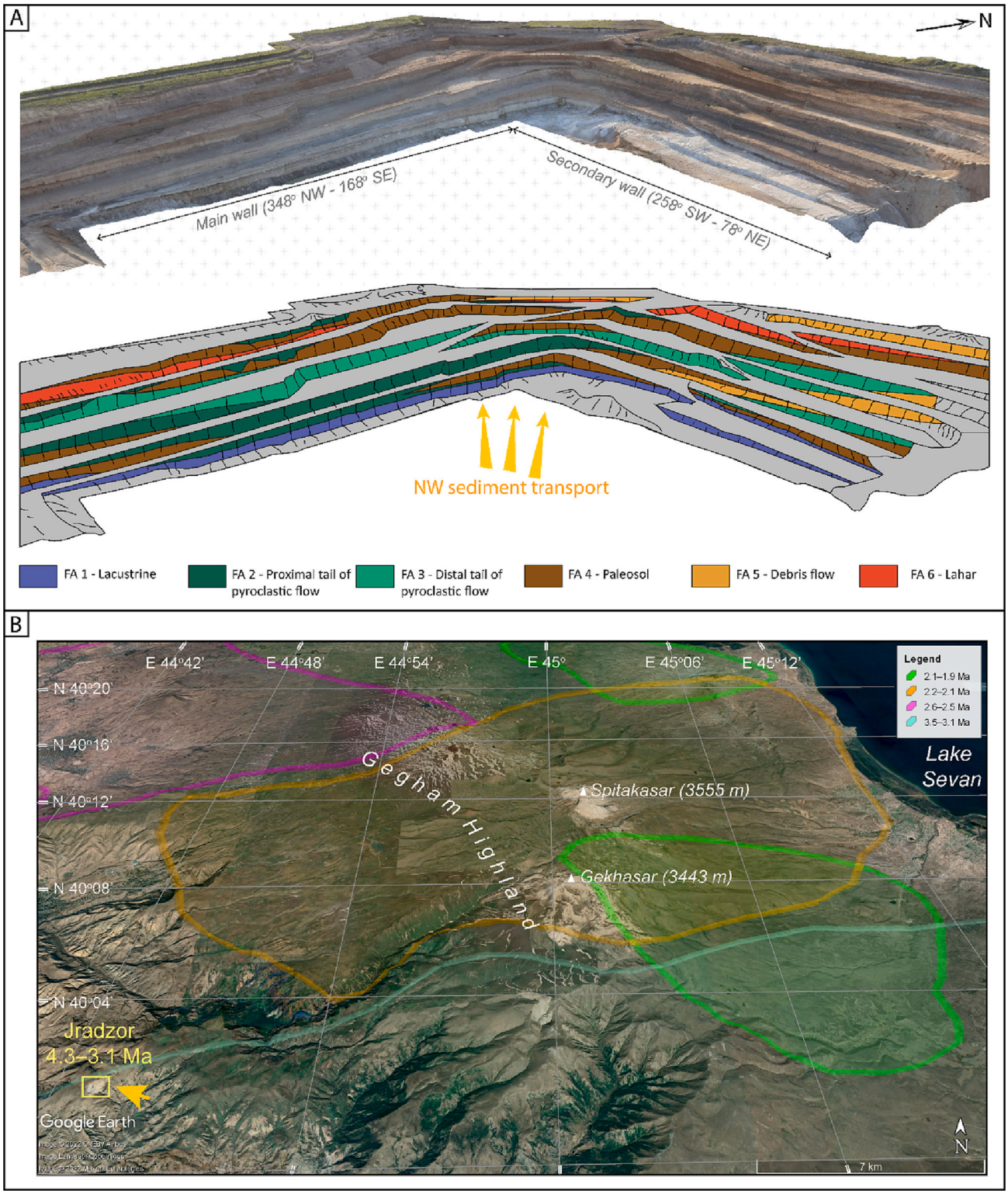

Fig. 9. A. Distribution of determined facies associations and sediment transport direction in the Jradzor section. B. Relations between the Jradzor section and surrounding volcanic fields being active during Plio–Pleistocene (Arutyunyan et al., 2007; Lebedev et al., 2021; Lebedev et al., 2018). The schematic distribution of volcanic fields is drawn according to Fig. 3 in Lebedev et al. (2021).

the lateral linua sinosa) of which is not clearly defined yet. Nevertheless, this issue requires further studies on extensive material from this lineage and different regions. Overall, the small mammal taxa indicate a referral of the fauna to the MN15. This biochronological assignment (at least for layers JZ-3 to JZ-6) is in perfect agreement to our results on absolute and relative dating (4.16–3.98 Ma, Table 2, Fig. 5).

5.2. Source volcano and regional volcanism

The Jradzor section is located on the SE margin of the Gegham volcanic ridge, which was the likely source of volcaniclastic deposits in the area. The Gegham-origin of pyroclastic density flows is supported by our observations on the inclination, geometry and lateral variations of pyroclastic incisions and debris flow beds that point to an overall NW-direction of the sediment transport (Fig. 9A).

The Geghama volcanic province is a volcanic field with abundant (strato-)volcanoes representing Late Miocene–Quaternary post-collisional magmatism (Lebedev et al., 2021; Meliksetian, 2018). Geochronological and geochemical studies on volcanic rocks (lavas) in the Geghama province subdivided volcanic activity into three major stages with long gaps in between: 1. Late Miocene–Early Pliocene (5.56–4.7 Ma); 2. Late Pliocene–Early Pleistocene (3.5–1.9 Ma); 3. Middle–Late Pleistocene (0.9–0.01 Ma) (Lebedev et al., 2021) (Fig. 9B).

The Jradzor locality, primarily built of volcaniclastic rocks, is located in the southern part of the Geghama volcanic province, whose volcanic activity was attributed by Lebedev et al. (2021) to Stage 2 (3.5–1.9 Ma) (Fig. 9B). The integrated age model and facies analysis of the Jradzor section show the maximum distribution of pyroclastic density flow deposits between 4.3 and 3.93 Ma (interval 11–37 m, Fig. 9B) and after ~3.5 Ma (45–57 m) with a palaeosol interval (37–45 m) potentially representing a period of volcanic quiescence. Our data suggest that volcanic activity in the region was still ongoing between the proposed stages I and II of Lebedev et al. (2021). Such contradiction may have been caused by the lack of attention to volcaniclastic deposits in the studies of regional volcanic geochemistry that usually focus on volcanic rocks (Arutyunyan et al., 2007; Lebedev et al., 2021; Lebedev et al., 2018). At the same time, volcaniclastic deposits play an equally important role as lava flows in understanding the evolution of regional volcanism, and thus, both need to be considered along with each other.

5.3. Palaeoenvironmental evolution and formation of fossil horizons in the Jradzor section

5.3.1. Debris avalanche and lake formation at around 4.3 Ma

The Jradzor section begins with a massive debris avalanche breccia that forms a hummocky-shaped hill in the southern part of the quarry and deepens towards its centre (Fig. 3W, 10A). Southern from the southern wall of the quarry, we observed an overlap of this breccia onto andesitic lava flow deposits. Considering the monogenic lithological content of the breccia, we assume that the debris avalanche resulted from an explosive eruption in the neighbouring volcano that destroyed the volcanic edifice and in the shape of avalanche blocked the valley facilitating the formation of a dammed lake (Fig. 10B).

The lacustrine phase is characterised by a thick diatomite package (FA1) – a biogenic deposit common for volcanic silica-rich substrate (Lindqvist and Lee, 2009). Geological exploration of the mine, held in the '60s of the last century, revealed diatomite reserves on an area of 0.26 km2, representing the minimal surface of the paleolake (Gulyan

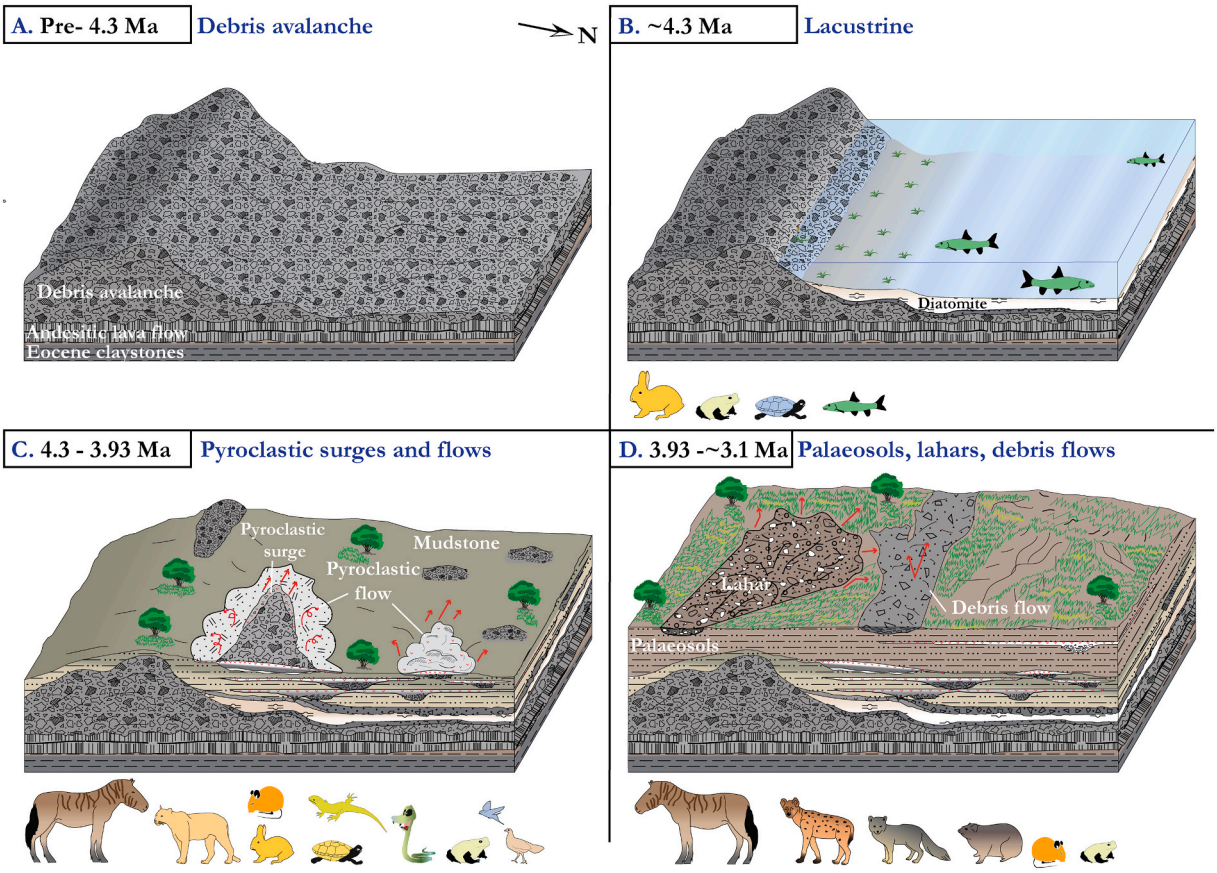

Fig. 10. Schematic 3D diagrams representing the evolution of palaeoenvironments, major faunal elements and depositional processes in the Jradzor section between 4.3 and ~3.1 Ma.

and Harutyunyan, 1966). The presence of cyprinid fish taxa suggests that the lake was hydrologically open or at least had an outflow down to the valley. The thinly-laminated part of the diatomite package (1.3–8 m) contains about 300–320 laminae per stratigraphic meter. Assuming the annual character of laminae and extrapolating this rate on the entire diatomite package (1.3–12.3 m, including the non-laminated upper part) result in duration of the lacustrine phase of about 3500 years. The lake disappearance was linked to its gradual sediment infill and desiccation, as suggested by the shallowing facies trend. At its final stage, the lake was strongly affected by pyroclastic flows represented by: tuffaceous sandstones and volcanic tephra on the lake margins; and highly erosive volcaniclastic breccia in its centre. The volcanic tuff, dated from the terminal stage of lacustrine deposits, has an age of 4.29 ± 0.09 Ma. Considering the rapid accumulation of the debris avalanche followed by a short lacustrine phase, we can consider the age of these events to be around 4.3 Ma.

5.3.2. Pyroclastic flows between 4.3 Ma and 3.93 Ma

Between 4.29 and 3.93 Ma, the depression of the former Jradzor lake was filled with pyroclastic density currents (Fig. 3H, 10C). The detailed facies analysis shows that within the FA2 (medium tail of pyroclastic flows, 19.5–29 m), the pyroclastic flows passing the outcrop area were still hot, not-expanded and highly erosive (Cas and Wright, 1987; Suthren, 1985). They were preceded by ground surges and followed by ash-cloud surges (Fisher, 1979) (Fig. 3K, 10C). The latter accumulated over larger areas than confined flows, mainly on the margins of the palaeotopographic depression. The deposits were consequently pedogenically modified as seen from abundant rootlets and aggregate structure. The presence of all three elements of pyroclastic deposits – ground surges, flows and ash-cloud surges, suggests a relative longitudinal proximity to a vent (Branney and Kokelaar, 2002). However, the lack of large boulders and the small thickness of pyroclastic deposits points to the rather medium tail of pyroclastic flows. Towards the top of the package (e.g. FA3), axial parts of pyroclastic flows are less

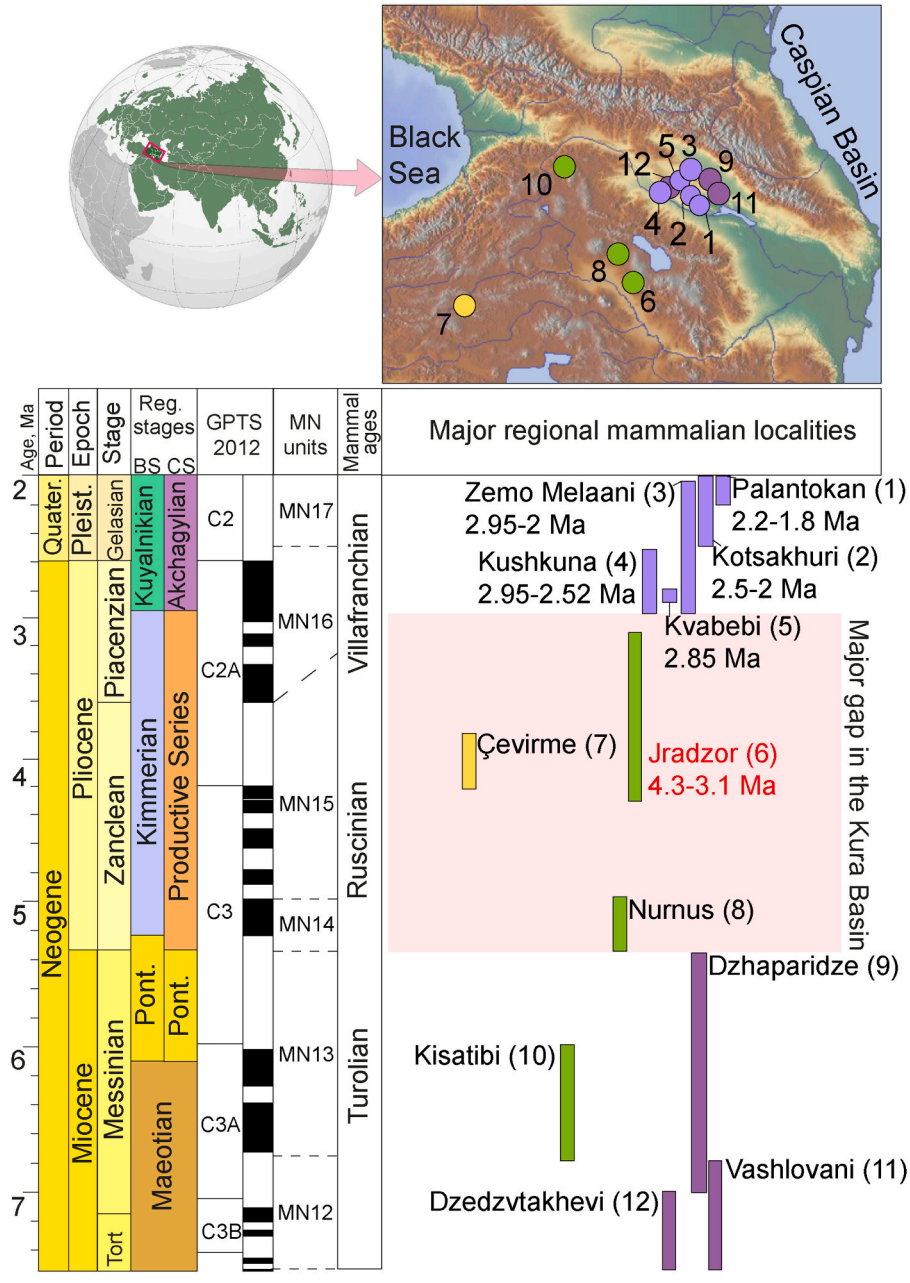

Fig. 11. Stratigraphic distribution of the Late Miocene to Early Pleistocene sites from the South Caucasus and eastern Turkey. The ages of the localities follow: 1. Palantakon (Sotnikova and Sablin, 1993); 2. Kotsakhuri (Bukhsianidze and Koiava, 2018); 3. Zemo Melaani: 2.95–2 Ma (Bukhsianidze and Koiava, 2018); 4. Kushkuna: 2.95–2.52 Ma (Lazarev et al., 2021); 5. Kvabebi: 2.85 Ma (Lazarev et al., 2021); 6. Jradzor: Present study; 7. Çevirm (Ayvazyan et al., 2019); 8. Nurnus (Melik-Adamyan, 2003); 9. Dzhaparidze (Meladze, 1985) 10. Kisatibi (Vangengeym et al., 1989); 11. Vashlovani (Bukhsianidze and Koiava, 2018); 12. Dzedzvtakhevi (Bukhsianidze and Koiava, 2018; Vekua and Trubikhin, 1988). Where available, absolute ages are also indicated. The semi-transparent red rectangle highlights the major gap in the Kura Basin, during which no sediments of this age are preserved (sensu Bukhsianidze and Koiava (2018)). The colouration of the stratigraphic coverages of vertebrate locality corresponds: dark purple represents Late Miocene sites from the Middle Kura Basin, light purple represents latest Pliocene to Early Pleistocene from the same basin; in green – sites from the volcaniclastic formation of the Lesser Caucasus and in yellow – site from the intramountainous basin in eastern Turkey. (For interpretation of the references to colour in this figure legend, the reader is referred to the web version of this article.)

pronounced, and the depositional processes become controlled by ash-cloud surges and stronger pedogenic modification.

The volcaniclastic interval in the Jradzor section contains most fossil horizons and most fossils of small-sized vertebrates (Table 2). The fossil remains are concentrated in both pyroclastic breccia and ash-cloud surge mudstones. Most of the taxa belong to groups with small mobility and/or live/hide in burrows, such as amphibians, reptiles, tortoises, lagomorphs and rodents. The high mortality of these near-surface-living groups likely resulted from a high erosive capacity of pyroclastic flows. Another intriguing aspect is the high number of bird remains. Despite the unclear number of taxa, high mortality among birds can be related either to a deadly depositional process of an ash-cloud surge or, to volcanic release of a CO_2-cloud (Franzen, 1985).

5.3.3. Palaeosols, minor pyroclastic flow and lahar between 3.93 and 3.1 Ma

After 3.93 Ma, the volcanic activity in the Jradzor area greatly diminished and depositional processes were controlled mainly by pedogenesis (FA4) (Fig. 3S, 3R, 10D), although, with rare pyroclastic flow still taking place (Fig. 9A). The palaeosols with rootlets, animal krotovinas (Fig. 3R, 3S) and volcanic rock particles represent a period of a relative volcanic standstill.

At 3.28 ± 0.05 Ma, the paedogenic record of the Jradzor has been disturbed by a cohesive debris flow of highly vesiculated pumice - a lahar (Fig.3 A1, 10D). Due to the high bulk density and velocity, lahars are considered one of the major hazards in volcanic areas (Tilling, 2014). In Jradzor, this catastrophic mudflow served as a trap for numerous large mammals such as hipparions, hyrax, raccoon dog, hyenas and bovids, all found in two lenses at the base of the lahar package. (Table 2, JZ-7). Besides large mammals, small-sized vertebrates, such as rodents and amphibians, have also been found.

Between 3.28 Ma and 3.1 Ma, depositional processes in Jradzor were controlled by long-lasting pedogenesis expressed as palaeosols with well-developed calcrete levels. The latter represents a soil horizon impregnated and cemented by paedogenic carbonates from a shallow groundwater table (Zamanian et al., 2016).

5.4. Fossil record of Jradzor and the rest of South Caucasus: palaeobiogeographic considerations

A combination of magnetostratigraphic, $^{40}Ar/^{39}Ar$ and biochronological age constraints allows plotting the Jradzor locality along with the other localities of the South Caucasus (Fig. 11).

The late Neogene fossil record of the South Caucasus has been mainly (geographically) limited to the Middle Kura Basin, where remarkably, despite the large numbers of other age localities, no localities of the Early Pliocene–early Late Pliocene exist in the area (Bukhsianidze and Koiava, 2018). Such a gap in the biotic and sedimentary record of the western and central parts of the Kura Basin resulted from the pre-Akchagylian denudation related to Late Miocene–Early Pliocene Caspian Sea lowstand and westward prograding convergence between the Lesser and the Greater Caucasus (Bukhsianidze and Koiava, 2018; Forte et al., 2010). As an alternative, the Pliocene biotic record can be potentially found in the volcanigenic formations of the South Caucasus (e.g., Goderdzi, Voghjaberd formations). So far, only two fossil localities, i.e. Nurnus and Kisatibi, are known in this area (Gabelaya, 1970; Melik-Adamyan et al., 1988) (Fig. 11). These two sites, as well as the site in this study, share similar sedimentary processes with lacustrine environments alternating with massive packages of volcaniclastic deposits. Further comparison, however, requires detailed sedimentological studies and well-constrained age models for those sites.

Comparison of the taxonomic richness between the South Caucasus fossil localities demonstrates, so far, the highest diversity in the Jradzor locality (Table 3).

Based on our preliminary palaeobiogeographic analysis of revealed taxa, we suggest the Jradzor locality as a key site for the palaeobiogeographic history of the South Caucasus region, especially having a transitional geographic position between Asia and Europe. Further, the aquatic forms found in the site will enable a better understanding of the regional evolution of the hydrological network. So, the earlier study on the fossil record of the doctor fish (*Garra* sp.) from JZ-1 (Vasilyan and Carnevale, 2013) demonstrate an ancient (pre-Pliocene) connection upstream of the Arax River Basin with the Mesopotamian River system, which is now part of the Caspian Sea Basin. The new age constraints will allow a better understanding of the evolution of the hydrological networks of the region.

Small mammals. A comparison of small mammalian assemblage from Jradzor with the same-age sites from Turkey, Greece and Bulgaria (Popov, 2004; Sen, 1998; Suata Alpaslan, 2010; Vasileiadou and Doukas, 2022; Vasileiadou and Sylvestrou, 2022a, 2022b) suggests complete agreement at the generic level and in most cases also on the species level. Moreover, except for *Deinsdorfia*, *Pliopetaurista*, *Neocricetodon*, and *Mesocricetus*, the same genera are also recorded from Ukrainian MN15 sites (Nesin, 2013). The absence of these taxa in Eastern Europe and the fact that the Spalacinae in the Ukrainian localities are placed in *Nannospalax*, while those in Turkey, Greece and Jradzor are placed in *Pliospalax* may be related to the different regional status of the study of these groups and to the problem of differentiation of *Nannospalax* and *Pliospalax* on the base of isolated teeth. It is also interesting to note that the Greek and Turkish small mammalian faunas of the MN14 show significant similarities with the MN15 faunas (Hordijk and de Bruijn, 2009; Sen, 1998; Suata Alpaslan, 2010; Vasileiadou and Doukas, 2022; Vasileiadou and Sylvestrou, 2022a, 2022b). These interregional similarities could suggest that in the Early Pliocene (MN14–15), relatively unimpeded faunal exchange was possible for small mammals both to the west (Western Asia, Southeastern Europe) and north (Eastern Europe) across the Caucasus.

Large mammals. The Jradzor site, together with the Polish record from Węże-1 (Ruscinain, MN15, Croitor and Stefaniak, 2009), potentially provides the earliest evidence of the dispersal of *Arvernoceros* from Asia westwards (from the Altai-Sayany Region according to Vislobokova, 2012 or from South Asia according to Croitor, 2018). The earliest

Table 3
Late Miocene to Early Pleistocene vertebrate localities from South Caucasus and eastern Turkey their taxonomic diversity. The numbers correspond to those in Fig. 11.

Nr.	Locality	Country	Age in Ma	Total number of taxa	Number of large mammals	Reference
1	Palantakon	Azerbaijan	2.2–1.8	15	15	Sotnikova and Sablin, 1993
2	Kotsakhuri	Georgia	2.5–2	10	7	Bukhsianidze and Koiava, 2018
3	Zemo Melaani	Georgia	2.95–2 Ma	6	6	Bukhsianidze and Koiava, 2018
4	Kushkuna	Georgia	2.95–2.52	13	11	Bukhsianidze and Koiava, 2018; Lazarev et al., 2021
5	Kvabebi	Georgia	2.85	28	25	Lazarev et al., 2021; Rook et al., 2017
6	Jradzor	Armenia	4.3–3.1	>49	13?	Present study
7	Çevirm	Turkey	4.1–3.9	4		Ayvazyan et al., 2019
8	Nurnus	Armenia	5–5.38	29		Melik-Adamyan, 2003
9	Dzhaparidze	Georgia	5.38–7	7	7	Bukhsianidze and Koiava, 2018; Meladze, 1985
10	Kisatibi	Georgia	6–6.8	6		Vangengeym et al., 1989
11	Vashlovani	Georgia	6.8–7.5	2	2	Bukhsianidze and Koiava, 2018
12	Dzedzvtakhevi	Georgia	7.5–7	10	9	Bukhsianidze and Koiava, 2018; Vekua and Trubikhin, 1988

probable record of the genus *Gazellospira* comes from Asia Minor (Çalta, MN15, Turkey; Bouvrain, 1998) and Central Europe (Csarnóta 2, MN15, Hungary; de Bruijn et al., 1992) and is the most common spiral-horned antelope of Western Eurasia until the late Villafranchian (MQ1). The presence of two different Caprinae (one largesize Caprinae (a probable Ovini) and another medium size taxon with ovibovine characters) attests range expansion of mountain animals from Asia – the Tibetan plateau and the peri-Tibet area (Wang et al., 2016) and highlights the biogeographic role of the Caucasus region as a faunal dispersal corridor.

The large mammalian forms include Palaearctic Pliocene species: *"Hipparion" fissurae, Pliocrocuta perrieri* and *Chasmaporthetes lunensis*. "*Hipparion*" cf. *fissurae* from Jradzor can undoubtedly be considered as among the last occurrences of Hipparionine through Eurasia (Cirilli et al., 2023; Cirilli et al., 2021), with notably *Plesiohipparion rocinantis* from Kvabebi (MN16; Georgia; (Bukhsianidze and Koiava, 2018)). Moreover, the record of "*Hipparion*" cf. *fissurae* in Jradzor can potentially represent the first record of the taxa in the South Caucasus and, at the same time, its most eastern occurrence. This statement, however, requires further clarification of the taxonomy of this Jradzor Hipparionine and its comparison with other Hipparion remains from the neighbouring regions.

6. Conclusion

Integration of sedimentological, palaeontological and geochronological data allowed us to reconstruct palaeoenvironments, faunal assemblages and mechanisms of the fossil horizon formation in the Jradzor section and place them in an accurate chronostratigraphic framework. The 57-m-thick Jradzor section comprises 19 fossiliferous horizons with >48 taxa distributed in various depositional settings – from lacustrine to pyroclastic density currents and palaeosols. A combination of $^{40}Ar/^{39}Ar$, magnetostratigraphic and biochronological dating methods date the Jradzor locality between 4.3 Ma and ~ 3.03 Ma and/or as MN15 zone.

Sedimentological analysis in combination with taphonomic observations, suggests that accumulations of small-size vertebrate fossil fauna (amphibians, reptiles, birds and mammals) were linked to catastrophic pyroclastic flows and ash-cloud surges concentrated in the axial part of the palaeotopographic depression. The lowermost fossil locality JZ-1, with complete fish remains, was formed in distal lacustrine settings, while the only locality with large mammal fauna (JZ-7) resides at the base of a sudden volcaniclastic debris flow - a lahar. The pyroclastic and volcaniclastic deposits in Jradzor were transported in the NW-direction, originating from the Geghama volcanic ridge, which was especially volcanically active between 4.3 Ma and ~ 3.93 Ma. A comparison with the other fossil assemblages from the region shows that Jradzor contains the highest number of vertebrates taxa (from both aquatic and continental environments/deposits) and fills up a crucial gap of the MN15 mammalian zone in the South Caucasus biotic record. In addition, our palaeobiogeographic analysis of the faunistic elements from the Jradzor suggests its stronger relationship with European faunas; however, a few exclusively Asian elements are also present.

Further, our study confirms that despite volcaniclastic deposits having a limited preservation potential, they often served as a natural trap for various faunal groups and, thus, should not be dismissed while studying the regional fossil record. The revealed fossil vertebrate faunas of the Jradzor locality are not only crucial for understanding of the regional evolution of the biotic record but also represent an essential tie point for the Eurasian palaeobiogeography.

Declaration of Competing Interest

The authors declare that they have no known competing financial interests or personal relationships that could have appeared to influence the work reported in this paper.

Data availability

All research data from this manuscript are stored in supplementary files

Acknowledgements

We would like to thank all participants in excavations at the Jradzor site since 2007. We also thank the JURASSICA Museum for financial support in the organisation of the International Palaeontological Field School in 2019 for the collection of fossils in the field. Special thanks due to: I. Gabrielyan (Yerevan) and S. Pipoyan (Yerevan) for assistance and encouragement during the earliest stages of the study of the site; to Iuliana Vasiliev for help with palaeomagnetic sampling in the field; to Wout Krijgsman (Utrecht) for improvements of the paper structure; to Gerald Mayr (Frankfurt am Main) for preliminary identification; to preparator of the JURASSICA Museum Renaud Roch for preparation of fossils both in the field and in the lab. We would also like to thank the staff of the diatomite mine for their hospitality, administrative and logistic support during all fieldworks. This manuscript would be sloppy and less structured without the help of the editor Falcon Lang (London) and three reviewers: Fabrizio Marra (Rome), Lars van den Hoek Ostende (Leiden) and anonymous reviewer. We are thankful to them for their great corrections and the time taken for the review.

Appendix A. Supplementary data

Supplementary data to this article can be found online at https://doi.org/10.1016/j.palaeo.2023.111685.

References

Adamia, S., Alania, V., Chabukiani, A., Chichua, G., Enukidze, O., Sadradze, N., 2010. Evolution of the late Cenozoic basins of Georgia (SW Caucasus): a review. Geol. Soc. Lond., Spec. Publ. 340, 239–259. https://doi.org/10.1144/SP340.11.

Adler, D.S., Bar-Yosef, O., Belfer-Cohen, A., Tushabramishvili, N., Boaretto, E., Mercier, N., Valladas, H., Rink, W.J., 2008. Dating the demise: neandertal extinction and the establishment of modern humans in the southern Caucasus. J. Hum. Evol. 55, 817–833. https://doi.org/10.1016/j.jhevol.2008.08.010.

Adler, D.S., Wilkinson, K.N., Blockley, S., Mark, D.F., Pinhasi, R., Schmidt-Magee, B.A., Nahapetyan, S., Mallol, C., Berna, F., Glauberman, P.J., Raczynski-Henk, Y., Wales, N., Frahm, E., Jöris, O., MacLeod, A., Smith, V.C., Cullen, V.L., Gasparian, B., 2014. Early Levallois technology and the Lower to Middle Paleolithic transition in the Southern Caucasus. Science (New York, N.Y.) 345, 1609–1613. https://doi.org/10.1126/science.1256484.

Allen, M.B., Kheirkhah, M., Neill, I., Emami, M.H., Mcleod, C.L., 2013. Generation of Arc and Within-plate Chemical Signatures in Collision Zone Magmatism: Quaternary Lavas from Kurdistan Province, Iran. J. Petrol. 54, 887–911. https://doi.org/10.1093/petrology/egs090.

Antonosyan, M., Seersholm, F.V., Grealy, A.C., Barham, M., Werndly, D., Margaryan, A., Cieślik, A., Stafford, T.W., Allentoft, M.E., Bunce, M., Yepiskoposyan, L., 2019. Ancient DNA shows high faunal diversity in the Lesser Caucasus during the late Pleistocene. Quat. Sci. Rev. 219, 102–111. https://doi.org/10.1016/j.quascirev.2019.07.012.

Arutyunyan, E.V., Lebedev, V.A., Chernyshev, I.V., Sagatelyan, A.K., 2007. Geochronology of Neogene-Quaternary volcanism of the Geghama Highland (Lesser Caucasus, Armenia). Dokl. Earth Sc. 416, 1042–1046. https://doi.org/10.1134/S1028334X07070136.

Avagyan, A., Shahidi, A., Sosson, M., Sahakyan, L., Galoyan, G., Muller, C., Vardanyan, S., Firouzi, K.B., Bosch, D., Danelian, T., Asatryan, G., Mkrtchyan, M., Shokri, M.A., 2017. New data on the tectonic evolution of the Khoy region, NW Iran. Geol. Soc. Lond., Spec. Publ. 428, 99–116. https://doi.org/10.1144/SP428.13.

Avakyan, T.A., 1963. Micropaleobotanical studies of the diatomites of the Jradzor locality. Proc. Acad. Sci. Armenian SSR Earth Sci. 5.

Avanesyan, M., 2014. Geological and structural features of Yerevan-Vedi graben-synclinory. PhD thesis, 162 pp.

Ayvazyan, A., Vasilyan, D., Böhme, M., 2019. Possible species-flock scenario for the evolution of the cyprinid genus *Capoeta* (Cypriniformes: Cyprinidae) within late Neogene lake systems of the armenian Highland. PloS One 14, e0215543. https://doi.org/10.1371/journal.pone.0215543.

Bar-Yosef, O., Belfer-Cohen, A., 2001. From Africa to Eurasia — early dispersals. Quat. Int. 75, 19–28. https://doi.org/10.1016/S1040-6182(00)00074-4.

Bernor, R.L., Koufos, G.D., Woodburne, M.O., Fortelius, M., 1996. The Evolutionary history and Biochronology of European and Southwest Asian Late Miocene and Pliocene Hipparionine Horses. In: Bernor, R.L., Fahlbusch, V., Mittmann, H.-W.

(Eds.), The Evolution of Western Eurasian Neogene Mammal Faunas. Columbia University Press, New York.
Bibi, F., 2011. Mio-pliocene faunal exchanges and african biogeography: the record of fossil bovids. PloS One 6, e16688. https://doi.org/10.1371/journal.pone.0016688.
Böhme, M., Spassov, N., Majidifard, M.R., Gärtner, A., Kirscher, U., Marks, M., Dietzel, C., Uhlig, G., El Atfy, H., Begun, D.R., Winklhofer, M., 2021. Neogene hyperaridity in Arabia drove the directions of mammalian dispersal between Africa and Eurasia. Commun. Earth Environ. 2 https://doi.org/10.1038/s43247-021-00158-y.
Bouvrain, G., 1998. Le gisement de vertébrés pliocènes de Çalta, Ankara, Turquie.: 10. Bovidae. In: Sen, S. (Ed.), Pliocene vertebrate locality of Çalta, Ankara, Turkey, vol. 20, pp. 467–485.
Branney, M.J., Kokelaar, P., 2002. Pyroclastic Density Currents and the Sedimentation of Ignimbrites. Geol. Soc. Lond. Mem. 27 https://doi.org/10.1144/GSL.MEM.2003.027.
Bukhsianidze, M., Koiava, K., 2018. Synopsis of the terrestrial vertebrate faunas from the Middle Kura Basin (Eastern Georgia and Western Azerbaijan, South Caucasus). Acta Palaeontol. Pol. 63 https://doi.org/10.4202/app.00499.2018.
Cas, R.A.F., Wright, J.V., 1987. Volcanic Successions Modern and Ancient. Springer, Netherlands, Dordrecht.
Čermák, S., 2007. New finds of *Ochotonoma csarnotana* (Lagomorpha, Ochotonidae) from the Pliocene of Hungary: a new look on the species. njgpa 246, 247–256. https://doi.org/10.1127/0077-7749/2007/0246-0247.
Čermák, S., 2010. The Late Miocene and Pliocene Ochotoninae (Lagomorpha, Mammalia) of Europe - the present state of knowledge. In: Nowakowski, D. (Ed.), Morphology and Systematics of Fossil Vertebrates. DN - Wrocław, Wrocław.
Čermák, S., Angelone, C., Sinitsa, M.V., 2015. New late Miocene *Alilepus* (Lagomorpha, Mammalia) from Eastern Europe - a new light on the evolution of the earliest Old World Leporinae. Bull. Geosci. 431–451 https://doi.org/10.3140/bull.geosci.1523.
Chough, S.K., 2013. Jeju Island. In: Geology and Sedimentology of the Korean Peninsula. Elsevier, pp. 291–303.
Cirilli, O., Bernor, R.L., Rook, L., 2021. New insights on the early Pleistocene equids from Roca-Neyra (France, Central Europe): implications for the *Hipparion* LAD and the Equus FAD in Europe. J. Paleontol. 95, 406–425. https://doi.org/10.1017/jpa.2020.99.
Cirilli, O., Pandolfi, L., Alba, D.M., Madurell-Malapeira, J., Bukhsianidze, M., Kordos, L., Lordkipanidze, D., Rook, L., Bernor, R.L., 2023. The last Plio-Pleistocene hipparions of Western Eurasia. A review with remarks on their taxonomy, paleobiogeography and evolution. Quat. Sci. Rev. 306, 107976 https://doi.org/10.1016/j.quascirev.2023.107976.
Colombero, S., Carnevale, G., 2016. Late Miocene (Turolian, MN13) squirrels from Moncucco Torinese, NW Italy. Compt. Rend. Palevol. 15, 515–526. https://doi.org/10.1016/j.crpv.2015.09.021.
Croitor, R., 2018. A Description of two New Species of the Genus *Rucervus* (Cervidae, Mammalia) from the early Pleistocene of Southeast Europe, with comments on Hominin and South Asian Ruminants Dispersals. Quaternary 1, 17. https://doi.org/10.3390/quat1020017.
Croitor, R., Stefaniak, K., 2009. Early Pliocene deer of Central and eastern european regions and inferred phylogenetic relationships. Pala 287, 1–39. https://doi.org/10.1127/pala/287/2009/1.
Dahlmann, T., 2001. Die Kleinsäuger der Unter-pliozänen Fundstelle Wölfersheim in der Wetterau (Mammalia: Lipotyphla, Chiroptera, Rodentia). In: Schweizerbart, Stuttgart, p. 128.
de Bruijn, H., Daams, R., Daxner-Höck, G., Fahlbusch, V., Ginsburg, L., Mein, P., Marles, J., Heinzmann, E., Mayhew, D.F., van der Meulen, A.J., Schmidt-Kittler, N., Antunes, M.T., 1992. Report of the RCMNS working group on fossil mammals, Reisensburg 1990. Newsl. Stratigr. 26, 65–118. https://doi.org/10.1127/nos/26/1992/65.
Dean, W.E., Fouch, T.D., 1983. Lacustrine environment. In: Scholle, P.A., Bebout, D., Moore, C. (Eds.), Carbonate Depositional Environments. American Association of Petroleum geologits Memoire.
Demeter, F., Bae, C.J., 2020. Dispersal Barriers into Southeast Asia during the late Pleistocene. Quat. Int. 563, 1–4. https://doi.org/10.1016/j.quaint.2020.09.035.
Derevianko, A., Anoykin, A., Kazansky, A., Matasova, G., 2015. New Data to Justify the Age of Early Paleolithic Artifacts of Rubas-1 Site (Seaside Dagestan). Izvasu. https://doi.org/10.14258/izvasu(2015)3.2-11.
Erbajeva, M.A., 1994. Phylogeny and evolution of Ochotonidae with emphasis on Asian ochotonids. Tokyo Natl. Sci. Mus. Monogr. 1–13.
Fejfar, O., Heinrich, W.D., Lindsay, E.H., 1998. In: Updating the Neogene Rodent biochronology in Europe. Mededelingen Nederlands Instituut voor Toegepaste Geowetenschappen TNO, pp. 533–553.
Fisher, R., 1953. Dispersion on a sphere. Proc. Royal Soc. A: Math. Phys. Eng. Sci. 217, 295–305.
Fisher, R.V., 1979. Models for pyroclastic surges and pyroclastic flows. J. Volcanol. Geotherm. Res. 6, 305–318. https://doi.org/10.1016/0377-0273(79)90008-8.
Fisher, R.V., Smith, G.A., 1991. Sedimentation in Volcanic Settings. SEPM (Society for Sedimentary Geology).
Forte, A.M., Cowgill, E., Bernardin, T., Kreylos, O., Hamann, B., 2010. Late Cenozoic deformation of the Kura fold-thrust belt, southern Greater Caucasus. Tectonophysics 122, 465–486. https://doi.org/10.1130/B26464.1.
Franzen, J.L., 1985. Exceptional preservation of Eocene vertebrates in the lake deposit of Grube Messel (West Germany). Phil. Trans. R. Soc. Lond. B 311, 181–186. https://doi.org/10.1098/rstb.1985.0150.
Gabelaya, T.D., 1970. New data on the fossil fishes from Kisatibi. Bull. Acad. Sci. Georgian SSR 59, 233–236.
Gabunia, L., Gabashvili, E., Vekua, A., Lordkipanidze, D., 2010. The late Miocene hominoid from Georgia. In: de Bonis, L., Koufos, G.D., Andrews, P. (Eds.), Hominoid Evolution and Climatic Change in Europe. Cambridge University Press, pp. 316–325.
Gabunia, L., Vekua, A., Lordkipanidze, D., Swisher, C.C., Ferring, R., Justus, A., Nioradze, M., Tvalchrelidze, M., Antón, S.C., Bosinski, G., Jöris, O., Lumley, M.A., Majsuradze, G., Mouskhelishvili, A., 2000. Earliest Pleistocene hominid cranial remains from Dmanisi, Republic of Georgia: taxonomy, geological setting, and age. Science (New York, N.Y.) 288, 1019–1025. https://doi.org/10.1126/science.288.5468.1019.
Gibert, C., Vignoles, A., Contoux, C., Banks, W.E., Barboni, D., Boisserie, J.-R., Chavasseau, O., Fluteau, F., Guy, F., Noûs, C., Otero, O., Sepulchre, P., Souron, A., Ramstein, G., 2022. Climate-inferred distribution estimates of mid-to-late Pliocene hominins. Glob. Planet. Chang. 210, 103756 https://doi.org/10.1016/j.gloplacha.2022.103756.
Gulyan, E.K., Harutyunyan, A.A., 1966. Jradzor diatomite site of the armenian SSR.: Reports of the Armenian Geological Fonds 1686, pp. 1–11.
Harrison, T., 2011. Paleontology and Geology of Laetoli: Human Evolution in Context. Springer, Netherlands, Dordrecht.
Haywood, A.M., Dowsett, H.J., Dolan, A.M., 2016. Integrating geological archives and climate models for the mid-Pliocene warm period. Nat. Commun. 7, 10646. https://doi.org/10.1038/ncomms10646.
Hordijk, K., de Bruijn, H., 2009. The succession of rodent faunas from the Mio/Pliocene lacustrine deposits of the Florina-Ptolemais-Servia Basin (Greece). Hellenic J. Geosci. 21–103.
Iurino, D.A., Bellucci, L., Schreve, D., Sardella, R., 2014. Exceptional soft tissue fossilization of a Pleistocene vulture (Gyps fulvus): new evidence for emplacement temperatures of pyroclastic flow deposits. Quat. Sci. Rev. 96, 180–187. https://doi.org/10.1016/j.quascirev.2014.04.024.
Jiang, B., Harlow, G.E., Wohletz, K., Zhou, Z., Meng, J., 2014. New evidence suggests pyroclastic flows are responsible for the remarkable preservation of the Jehol biota. Nat. Commun. 5, 3151. https://doi.org/10.1038/ncomms4151.
Jiang, D., Klaus, S., Zhang, Y.-P., Hillis, D.M., Li, J.-T., 2019. Asymmetric biotic interchange across the Bering land bridge between Eurasia and North America. Natl. Sci. Rev. 6, 739–745. https://doi.org/10.1093/nsr/nwz035.
Joannin, S., Cornée, J.-J., Münch, P., Fornari, M., Vasiliev, I., Krijgsman, W., Nahapetyan, S., Gabrielyan, I., Ollivier, V., Roiron, P., Chataigner, C., 2010. Early Pleistocene climate cycles in continental deposits of the Lesser Caucasus of Armenia inferred from palynology, magnetostratigraphy, and 40Ar/39Ar dating. Earth Planet. Sci. Lett. 291, 149–158. https://doi.org/10.1016/j.epsl.2010.01.007.
Kandel, A.W., Gasparyan, B., Allué, E., Bigga, G., Bruch, A.A., Cullen, V.L., Frahm, E., Ghukasyan, R., Gruwier, B., Jabbour, F., Miller, C.E., Taller, A., Vardazaryan, V., Vasilyan, D., Weissbrod, L., 2017. The earliest evidence for Upper Paleolithic occupation in the armenian Highlands at Aghitu-3 Cave. J. Hum. Evol. 110, 37–68. https://doi.org/10.1016/j.jhevol.2017.05.010.
Karapetyan, K.I., Adamyan, A.A., 1973. Recent volcanism in some areas of the Armenian SSR [in Russian]. Academy of Sciences of the Armenian SSR, Yerevan.
King, R.F., 1955. The remanent magnetism of artificially deposited sediments. Geophys. J. Int. 7, 115–134.
Krijgsman, W., Tesakov, A., Yanina, T., Lazarev, S., Danukalova, G., van Baak, C., Agustí, J., Alçiçek, M.C., Aliyeva, E., Bista, D., Bruch, A., Büyükmeriç, Y., Bukhsianidze, M., Flecker, R., Frolov, P., Hoyle, T.M., Jorissen, E.L., Kirscher, U., Koriche, S.A., Kroonenberg, S.B., Lordkipanidze, D., Oms, O., Rausch, L., Singarayer, J., Stoica, M., van de Velde, S., Titov, V.V., Wesselingh, F.P., 2019. Quaternary time scales for the Pontocaspian domain: Interbasinal connectivity and faunal evolution. Earth Sci. Rev. 188, 1–40. https://doi.org/10.1016/j.earscirev.2018.10.013.
Kuiper, K.F., Deino, A., Hilgen, F.J., Krijgsman, W., Renne, P.R., Wijbrans, J.R., 2008. Synchronizing rock clocks of Earth history. Science (New York, N.Y.) 320, 500–504. https://doi.org/10.1126/science.1154339.
Lazarev, S., Kuiper, K.F., Oms, O., Bukhsianidze, M., Vasilyan, D., Jorissen, E.L., Bouwmeester, M.J., Aghayeva, V., van Amerongen, A.J., Agustí, J., Lordkipanidze, D., Krijgsman, W., 2021. Five-fold expansion of the Caspian Sea in the late Pliocene: New and revised magnetostratigraphic and 40Ar/39Ar age constraints on the Akchagylian Stage. Glob. Planet. Chang. 103624 https://doi.org/10.1016/j.gloplacha.2021.103624.
Lazarev, S., de Leeuw, A., Stoica, M., Mandic, O., van Baak, C., Vasiliev, I., Krijgsman, W., 2020. From Khersonian drying to Pontian "flooding": late Miocene stratigraphy and palaeoenvironmental evolution of the Dacian Basin (Eastern Paratethys). Glob. Planet. Chang. 192, 103224 https://doi.org/10.1016/j.gloplacha.2020.103224.
Lebedev, V.A., Bubnov, S.N., Dudauri, O.Z., Vashakidze, G.T., 2008. Geochronology of Pliocene volcanism in the Dzhavakheti Highland (the Lesser Caucasus). Part 1: Western part of the Dzhavakheti Highland. Stratigr. Geol. Correl. 16, 204–224. https://doi.org/10.1134/S0869593808020081.
Lebedev, V.A., Chernyshev, I.V., Sagatelyan, A.K., Goltsman, Y.V., Oleinikova, T.I., 2018. Miocene-Pliocene Volcanism of Central Armenia: Geochronology and the Role of AFC Processes in Magma Petrogenesis. J. Volcanolog. Seismol. 12, 310–331. https://doi.org/10.1134/S0742046318050056.
Lebedev, V.A., Goltsman, Y.V., Oleinikova, T.I., Parfenov, A.V., Yakushev, A.I., 2021. The Pliocene Post-Collisional Volcanism of Central Armenia: Isotope-Geochronology and Geochemical Evolution of Magmatic Melts. Petrology 29, 627–656. https://doi.org/10.1134/S0869591121060059.
Lechmann, A., Burg, J.-P., Ulmer, P., Guillong, M., Faridi, M., 2018. Metasomatized mantle as the source of Mid-Miocene-Quaternary volcanism in NW-Iranian Azerbaijan: Geochronological and geochemical evidence. Lithos 304–307, 311–328. https://doi.org/10.1016/j.lithos.2018.01.030.

Lee, J.-Y., Marti, K., Severinghaus, J.P., Kawamura, K., Yoo, H.-S., Lee, J.B., Kim, J.S., 2006. A redetermination of the isotopic abundances of atmospheric Ar. Geochim. Cosmochim. Acta 70, 4507–4512. https://doi.org/10.1016/j.gca.2006.06.1563.
Lindqvist, J.K., Lee, D.E., 2009. High-frequency paleoclimate signals from Foulden Maar, Waipiata Volcanic Field, southern New Zealand: an early Miocene varved lacustrine diatomite deposit. Sediment. Geol. 222, 98–110. https://doi.org/10.1016/j.sedgeo.2009.07.009.
Lordkipanidze, D., Ponce de León, M.S., Margvelashvili, A., Rak, Y., Rightmire, G.P., Vekua, A., Zollikofer, C.P.E., 2013. A complete skull from Dmanisi, Georgia, and the evolutionary biology of early Homo. Science (New York, N.Y.) 342, 326–331. https://doi.org/10.1126/science.1238484.
Martin-Merino, G., Roverato, M., Almeida, R., 2021. Volcaniclastic lacustrine sedimentation in the Pleistocene Guayllabamba intermontane basin in the Ecuadorian Andes. Geol. Soc. Lond. Spec. Publ. https://doi.org/10.1144/SP520-2021-66. SP520-2021-66.
Mein, P., 1970. Les Sciuropteres (Mammalia, Rodentia) Neogenes d'Europe occidentale. Geobios 3, 7–77. https://doi.org/10.1016/S0016-6995(70)80001-8.
Meladze, G.K., 1985. In: Obzor Gipparionovyh Faun Kavkaza. Mecsniereba, Tbilisi, p. 75.
Melik-Adamyan, G.U., 2003. Stratigraphy and Paleogeography of Pliocene and Lower Neopleistocene of Central and Northwestern Armenia Based on Fauna of Land Vertebrates. Abridged thesis of Candidate of Science, Yerevan.
Melik-Adamyan, H.H., Kurochkin, E.N., Chkhikvadze, V.M., 1988. New data on the Pliocene age fauna from Nurnus, Armenia and a description of the extinct subspecies of the Caspian turtle. Vestnik Zool. 6, 71–74.
Meliksetian, K.B., 2018. Generation of collision magmas on the example of a Quaternary volcanism in the territory of Armenia and volcanic hazard.: [In Russian]. Doctoral thesis. Yerevan.
Miall, A.D., 1996. The geology of fluvial deposits: Sedimentary facies, basin analysis, and petroleum geology / Andrew D. Miall. Springer, Berlin, London.
Min, K., Mundil, R., Renne, P.R., Ludwig, K.R., 2000. A test for systematic errors in $^{40}Ar/^{39}Ar$ geochronology through comparison with U/Pb analysis of a 1.1-Ga rhyolite. Geochim. Cosmochim. Acta 64, 73–98.
Mullender, T.A.T., Velzen, A.J., Dekkers, M.J., 1993. Continuous drift correction and separate identification of ferrimagnetic and paramagnetic contributions in thermomagnetic runs. Geophys. J. Int. 114, 663–672. https://doi.org/10.1111/j.1365-246X.1993.tb06995.x.
Nakhutsrishvili, G., Zazanashvili, N., Batsatsashvili, K., Montalvo Mancheno, C.S., 2015. Colchic and Hyrcanian forests of the Caucasus: similarities, differences and conservation status. Fl. Medit. 25 https://doi.org/10.7320/FlMedit25SI.185.
Navasardyan, G.K., 2006. Petrographic and petrochemical properties of late collisional volcanism in the Gegham highland: [in Russian]. In: , 3. Izvestiya of the National Academy of Science of Armenian, pp. 10–19.
Neill, I., Meliksetian, K., Allen, M.B., Navasardyan, G., Kuiper, K., 2015. Petrogenesis of mafic collision zone magmatism: the armenian sector of the Turkish-Iranian Plateau. Chem. Geol. 403, 24–41. https://doi.org/10.1016/j.chemgeo.2015.03.013.
Nesin, V.A., 2013. Neogene Murinae (Rodentia, Muridae) of Ukraine. Universytetskaya kniga, Sumy.
Nesin, V.A., Storch, G., 2004. Neogene Murinae of Ukraine (Mammalia, Rodentia). Senckenb. Lethaea 84, 351–365. https://doi.org/10.1007/BF03043476.
Nikogosian, I.K., Bracco Gartner, A.J., Mason, P.R., van Hinsbergen, D.J., Kuiper, K.F., Kirscher, U., Matveev, S., Grigoryan, A., Grigoryan, E., Israyelyan, A., van Bergen, M. J., Koornneef, J.M., Wijbrans, J.R., Davies, G.R., Meliksetian, K., 2023. The South armenian Block: Gondwanan origin and Tethyan evolution in space and time. Gondwana Res. 121, 168–195. https://doi.org/10.1016/j.gr.2023.03.023.
O'Dea, A., Lessios, H.A., Coates, A.G., Eytan, R.I., Restrepo-Moreno, S.A., Cione, A.L., Collins, L.S., de Queiroz, A., Farris, D.W., Norris, R.D., Stallard, R.F., Woodburne, M. O., Aguilera, O., Aubry, M.-P., Berggren, W.A., Budd, A.F., Cozzuol, M.A., Coppard, S.E., Duque-Caro, H., Finnegan, S., Gasparini, G.M., Grossman, E.L., Johnson, K.G., Keigwin, L.D., Knowlton, N., Leigh, E.G., Leonard-Pingel, J.S., Marko, P.B., Pyenson, N.D., Rachello-Dolmen, P.G., Soibelzon, E., Soibelzon, L., Todd, J.A., Vermeij, G.J., Jackson, J.B.C., 2016. Formation of the Isthmus of Panama. Sci. Adv. 2, e1600883 https://doi.org/10.1126/sciadv.1600883.
O'Regan, H.J., Turner, A., Bishop, L.C., Elton, S., Lamb, A.L., 2011. Hominins without fellow travellers? First appearances and inferred dispersals of Afro-Eurasian large-mammals in the Plio-Pleistocene. Quat. Sci. Rev. 30, 1343–1352. https://doi.org/10.1016/j.quascirev.2009.11.028.
Pe-Piper, G., Piper, D.J., Zouros, N., Anastasakis, G., 2019. Age, stratigraphy, sedimentology and tectonic setting of the Sigri Pyroclastic Formation and its fossil forests, early Miocene, Lesbos, Greece. Basin Res. 31, 1178–1197. https://doi.org/10.1111/bre.12365.
Pietsch, D., 2013. Krotovinas — soil archives of steppe landscape history. Catena 104, 257–264. https://doi.org/10.1016/j.catena.2012.12.003.
Ponomarenko, D., Ponomarenko, E., 2019. Describing krotovinas: a contribution to methodology and interpretation. Quat. Int. 502, 238–245. https://doi.org/10.1016/j.quaint.2018.05.037.
Popov, V.V., 2004. Pliocene small mammals (Mammalia, Lipotyphla, Chiroptera, Lagomorpha, Rodentia) from Muselievo (North Bulgaria). Geodiversitas 23, 403–491.
Posamentier, H.W., Walker, R.G., 2006. Facies Models Revisited. SEPM (Society for Sedimentary Geology).
Raaf, J.F.M., Boersma, J.R., Gelder, A., 1977. Wave-generated structures and sequences from a shallow marine succession, lower Carboniferous, County Cork, Ireland. Sedimentology 24, 451–483. https://doi.org/10.1111/j.1365-3091.1977.tb00134.x.
Raffi, I., Wade, B.S., Pälike, H., Beu, A.G., Cooper, R., Crundwell, M.P., Krijgsman, W., Moore, T., Raine, I., Sardella, R., Vernyhorova, Y.V., 2020. The Neogene Period. Geol. Time Scale 2020, 1141–1215.
Reading, H.G., 1996. Sedimentary environments: Processes, facies, and stratigraphy. In: Reading, H.G. (Ed.), 3rd ed. Blackwell Science, Cambridge, Mass., Oxford.
Reumer, J., 1984. Ruscinian and early Pleistocene Soricidae (Insectivora, Mammalia) from Tegelen (The Netherlands) and Hungary. Scr. Geol. 1–173.
Rodríguez-Sedano, L.A., Sarocchi, D., Caballero, L., Borselli, L., Ortiz-Rodríguez, A.J., Cerca-Ruiz, M.F., Moreno-Chávez, G., Franco Ramos, O., 2022. Post-eruptive lahars related to the 1913 eruption in La Lumbre Ravine, Volcán de Colima, Mexico: the influence of ravine morphometry on flow dynamics. J. Volcanol. Geotherm. Res. 421, 107423 https://doi.org/10.1016/j.jvolgeores.2021.107423.
Rolland, Y., 2017. Caucasus collisional history: Review of data from East Anatolia to West Iran. Gondwana Res. 49, 130–146. https://doi.org/10.1016/j.gr.2017.05.005.
Rolland, Y., Hässig, M., Bosch, D., Bruguier, O., Melis, R., Galoyan, G., Topuz, G., Sahakyan, L., Avagyan, A., Sosson, M., 2020. The East Anatolia-Lesser Caucasus ophiolite: an exceptional case of large-scale obduction, synthesis of data and numerical modelling. Geosci. Front. 11, 83–108. https://doi.org/10.1016/j.gsf.2018.12.009.
Rook, L., Bartolini Lucenti, S., Bukhsianidze, M., Lordkipanidze, D., 2017. The Kvabebi Canidae record revisited (late Pliocene, Sighnaghi, eastern Georgia). J. Paleontol. 91, 1258–1271. https://doi.org/10.1017/jpa.2017.73.
Rzebik-Kowalska, B., 1994. The Plio-Pleistocene patterns of distribution of the Soricidae in Poland. In: Merritt, J.F., Kirkland, G.L., Rose, R.K. (Eds.), Advances in the Biology of Shrews. Pittsburgh.
Sáez, A., Valero-Garcés, B.L., Moreno, A., Bao, R., Pueyo, J.J., González-Sampériz, P., Giralt, S., Taberner, C., Herrera, C., Gibert, R.O., 2007. Lacustrine sedimentation in active volcanic settings: the late Quaternary depositional evolution of Lake Chungará (northern Chile). Sedimentology 54, 1191–1222. https://doi.org/10.1111/j.1365-3091.2007.00878.x.
Sahakyan, L., Bosch, D., Sosson, M., Avagyan, A., Galoyan, G., Rolland, Y., Bruguier, O., Stepanyan, Z., Galland, B., Vardanyan, S., 2017. Geochemistry of the Eocene magmatic rocks from the Lesser Caucasus area (Armenia): evidence of a subduction geodynamic environment. Geol. Soc. Lond., Spec. Publ. 428, 73–98. https://doi.org/10.1144/SP428.12.
Sasaki, H., Sasaki, Y., Saito-Kato, M., Naruse, H., Yumi, M., Ishihara, Y., 2016. Stratigraphic variations in lacustrine sediment gravity-flow deposits intercalated in varved diatomite: an example from the Hiruzenbara Formation, Okayama Prefecture, Southwest Japan. Quat. Int. 397, 208–222. https://doi.org/10.1016/j.quaint.2015.08.032.
de Schepper, S., Gibbard, P.L., Salzmann, U., Ehlers, J., 2014. A global synthesis of the marine and terrestrial evidence for glaciation during the Pliocene Epoch. Earth Sci. Rev. 135, 83–102. https://doi.org/10.1016/j.earscirev.2014.04.003.
Sen, S., 1977. La faune de rongeurs pliocenes de Calm (Ankara, Turquie). Bull. Mus. Natl. d'Hist. Nat. Sci. Terre 61, 89–171.
Sen, S., 1998. Pliocene vertebrate locality of Çalta, Ankara, Turkey.: 4. Rodentia and Lagomorpha. In: Sen, S. (Ed.), Pliocene vertebrate locality of Çalta, Ankara, Turkey, pp. 359–378.
Sen, S., Sarica, N., 2011. Middle-late Miocene spalacidae (Mammalia) from western Anatolia, and the phylogeny of the family. Yerbilimleri 21–50.
Siebert, L., 1984. Large volcanic debris avalanches: Characteristics of source areas, deposits, and associated eruptions. J. Volcanol. Geotherm. Res. 22, 163–197. https://doi.org/10.1016/0377-0273(84)90002-7.
Skandalos, P., Lansing, K., Demirel, F.A., Alçiçek, M.C., Mayda, S., Dieleman, F., van den Ostende, L.W.H., 2023. Early Pliocene Arvicolinae and Cricetinae from the locality of Afşar, western Turkey. Turk. J. Earth Sci. https://doi.org/10.55730/1300-0985.1826.
Smith, G.A., 1986. Coarse-grained nonmarine volcaniclastic sediment: Terminology and depositional process. Geol. Soc. Am. Bull. 97, 1. https://doi.org/10.1130/0016-7606(1986)97<1:CNVSTA>2.0.CO;2.
Sosson, M., Rolland, Y., Müller, C., Danelian, T., Melkonyan, R., Kekelia, S., Adamia, S., Babazadeh, V., Kangarli, T., Avagyan, A., Galoyan, G., Mosar, J., 2010. Subductions, obduction and collision in the Lesser Caucasus (Armenia, Azerbaijan, Georgia), new insights. Geol. Soc. Lond., Spec. Publ. 340, 329–352. https://doi.org/10.1144/SP340.14.
Sotnikova, M.V., Sablin, M.V., 1993. The late Villafranchian association of carnivorous mammals from the locality Palan-Tyukan. In: , 249. Trudy Zoologičeskogo Instituta Akademii Nauk SSSR, pp. 134–145.
Suata Alpaslan, F., 2010. The Paleoecology of the continental early Pliocene of the eastern Mediterranean a construction based on rodents. In: Cumhuriyet Üniversitesi Fen-Edebiyat Fakültesi fen Bilimleri Dergisi, p. 31.
Sugden, P., Meliksetian, K., Savov, I.P., Barfod, D., Wilson, M., Connor, C., Navasardyan, G., Grigoryan, E., Manucharyan, D., 2021. Post-collisional shift from polygenetic to monogenetic volcanism revealed by new 40Ar/39Ar ages in the southern Lesser Caucasus (Armenia). J. Volcanol. Geotherm. Res. 412, 107192 https://doi.org/10.1016/j.jvolgeores.2021.107192.
Sugden, P.J., Savov, I.P., Wilson, M., Meliksetian, K., Navasardyan, G., Halama, R., 2019. The Thickness of the Mantle Lithosphere and Collision-Related Volcanism in the Lesser Caucasus. J. Petrol. 60, 199–230. https://doi.org/10.1093/petrology/egy111.
Sulpizio, R., Zanchetta, G., Demi, F., Di Vito, M.A., Pareschi, M.T., Santacroce, R., 2006. The Holocene syneruptive volcaniclastic debris flows in the Vesuvian area: Geological data as a guide for hazard assessment. In: Siebe, C., MacíasGerardo, J.L., Aguirre-Díaz, J. (Eds.), Neogene-Quaternary Continental Margin Volcanism: A perspective from México. Geological Society of America.
Suthren, R.J., 1985. Facies analysis of volcaniclastic sediments: a review. Geol. Soc. Lond., Spec. Publ. 18, 123–146. https://doi.org/10.1144/GSL.SP.1985.018.01.07.
Sylvestrou, I.A., Kostopoulos, D.S., 2007. *Pseudomeriones megistos* nov. sp. (Gerbillinae, Mammalia) from the latest Miocene of Northern Greece and its phylogenetic

relationships. Geobios 40, 833–848. https://doi.org/10.1016/j.geobios.2006.04.007.
Tabor, N.J., Myers, T.S., Michel, L.A., 2017. Sedimentologist's Guide for Recognition, Description, and Classification of Paleosols. In: Terrestrial Depositional Systems. Elsevier, pp. 165–208.
Tarkhnishvili, D., 2014. Historical Biogeography of the Caucasus. Nova.
Tate, M.P., Wilson, M., 1988. Emplacement mechanism and lateral correlation of pyroclastic flow and surge deposits in northen St Kitts, Lesser Antilles. J. Geol. Soc. 145, 553–562. https://doi.org/10.1144/gsjgs.145.4.0553.
Tauxe, L., Kent, D.V., 2004. A Simplified Statistical Model for the Geomagnetic Field and the Detection of Shallow Bias in Paleomagnetic Inclinations: Was the Ancient magnetic Field Dipolar? In: Channell, J., Kent, D.V., Lowrie, W., Meert, J.G. (Eds.), Timescales of the Paleomagnetic Field. American Geophysical Union, Washington, D. C, pp. 101–115.
Tilling, R.I., 2014. Volcanic Hazards☆. In: Reference Module in Earth Systems and Environmental Sciences. Elsevier.
Tucker, M.E., 2012. Sedimentary Rocks in the Field: a Practical Guide. Environ. Eng. Geosci. 18, 401–402. https://doi.org/10.2113/gseegeosci.18.4.401-b.
van Hinsbergen, D.J., Torsvik, T.H., Schmid, S.M., Maţenco, L.C., Maffione, M., Vissers, R.L., Gürer, D., Spakman, W., 2020. Orogenic architecture of the Mediterranean region and kinematic reconstruction of its tectonic evolution since the Triassic. Gondwana Res. 81, 79–229. https://doi.org/10.1016/j.gr.2019.07.009.
Vangengeym, E.A., Gabuniya, L.K., Pevzner, M.A., Tsiskarishvili, G.V., 1989. The stratigraphic position of the hipparion -FAUNA sites of transcaucasia in the light of magnetostratigraphY. Int. Geol. Rev. 31, 914–921. https://doi.org/10.1080/00206818909465944.
Vasileiadou, K., Doukas, C.S., 2022. The Fossil Record of Insectivores (Mammalia: Eulipotyphla) in Greece. In: Vlachos, E. (Ed.), Fossil Vertebrates of Greece, Vol. 2. Springer International Publishing, Cham, pp. 33–92.
Vasileiadou, K., Sylvestrou, I., 2022a. The Fossil Record of Hares, Rabbits, and Pikas (Mammalia: Lagomorpha) in Greece. In: Vlachos, E. (Ed.), Fossil Vertebrates of Greece, Vol. 1. Springer International Publishing, Cham, pp. 611–637.
Vasileiadou, K., Sylvestrou, I., 2022b. The Fossil Record of Rodents (Mammalia: Rodentia) in Greece. In: Vlachos, E. (Ed.), Fossil Vertebrates of Greece, Vol. 1. Springer International Publishing, Cham, pp. 407–610.
Vasiliev, I., van der Meer, M.T., Stoica, M., Krijgsman, W., Reichart, G.-J., Lazarev, S., Butiseacă, G.A., Niedermeyer, E.M., Aliyeva, E., van Baak, C.G., Mulch, A., 2022. Biomarkers reveal two paramount Pliocene-Pleistocene connectivity events in the Caspian Sea Basin. Palaeogeogr. Palaeoclimatol. Palaeoecol. 587, 110802 https://doi.org/10.1016/j.palaeo.2021.110802.
Vasilyan, D., 2008a. A new fossil species of dace *Leuciscus (Telestes)* cf. *souffia* Risso, 1826 from the Pleistocene sediments of the Ararat depression of Armenia. Biol. J. Armenia 60, 113–117.
Vasilyan, D., 2008b. The fishes of Pliocene-Pleistocene of Armenia and their sense for palaeoclimatological studies. Bull. MANEB 13, 60–65.
Vasilyan, D., Bukhsianidze, M., 2020. The fossil record of the genus *Varanus* from the Southern Caucasus (Armenia, Georgia). PeerJ 8, e8322. https://doi.org/10.7717/peerj.8322.
Vasilyan, D., Carnevale, G., 2013. The Afro-asian labeonine genus *Garra* Hamilton, 1822 (Teleostei, Cyprinidae) in the Pliocene of Central Armenia: Palaeoecological and palaeobiogeographical implications. J. Asian Earth Sci. 62, 788–796. https://doi.org/10.1016/j.jseaes.2012.11.033.
Vekua, A.K., Trubikhin, V.M., 1988. New site of fossil mammals in eastern Georgia: [in russian with georgian and English abstract]. Soobšeniâ Akademii Nauk Gruzinskoj SSR 132, 197–200.
Vereshchagin, V.N. (Ed.), 1982. Stratigraphic Dictionary of the USSR: Paleogene, Neogene, Quaternary System. Nedra, Leningrad.
Vislobokova, I.A., 2012. Giant deer: Origin, evolution, role in the biosphere. Paleontol. J. 46, 643–775. https://doi.org/10.1134/S0031030112070027.
Wang, X., Li, Q., Takeuchi, G.T., 2016. Out of Tibet: an early sheep from the Pliocene of Tibet, Protovis himalayensis, genus and species nov. (Bovidae, Caprini), and origin of Ice Age mountain sheep. J. Vertebr. Paleontol. 36, e1169190 https://doi.org/10.1080/02724634.2016.1169190.
Wohletz, K.H., Sheridan, M.F., 1979. A model of pyroclastic surge. In: Ash-Flow Tuffs, vol. 180. Geological Society of America, pp. 177–194.
Yi, J., Wang, P.-J., Shan, X.-L., Wang, H.-F., Sun, S., Chen, H., 2019. Lahar deposits generated after the Millennium eruption of the Changbaishan Tianchi volcano in the Erdaobaihe River system, China. J. Volcanol. Geotherm. Res. 380, 1–18. https://doi.org/10.1016/j.jvolgeores.2019.05.003.
Zamanian, K., Pustovoytov, K., Kuzyakov, Y., 2016. Pedogenic carbonates: Forms and formation processes. Earth Sci. Rev. 157, 1–17. https://doi.org/10.1016/j.earscirev.2016.03.003.
Zanon, V., Pacheco, J., Pimentel, A., 2009. Growth and evolution of an emergent tuff cone: Considerations from structural geology, geomorphology and facies analysis of São Roque volcano, São Miguel (Azores). J. Volcanol. Geotherm. Res. 180, 277–291. https://doi.org/10.1016/j.jvolgeores.2008.09.018.
Zouhri, S., Bensalmia, A., 2005. Révision systématique des *Hipparion* sensu lato (Perissodactyla, Equidae) de l'Ancien Monde. Estud. Geol. 61, 61–99. https://doi.org/10.3989/EGEOL.05611-243.